# RF COIL DESIGN FOR MULTI-FREQUENCY MAGNETIC RESONANCE IMAGING AND SPECTROSCOPY

A Thesis

by

ARASH DABIRZADEH

Submitted to the Office of Graduate Studies of
Texas A&M University
in partial fulfillment of the requirements for the degree of

MASTER OF SCIENCE

December 2008

Major Subject: Electrical Engineering

# RF COIL DESIGN FOR MULTI-FREQUENCY MAGNETIC RESONANCE IMAGING AND SPECTROSCOPY

A Thesis

by

ARASH DABIRZADEH

Submitted to the Office of Graduate Studies of
Texas A&M University
in partial fulfillment of the requirements for the degree of

MASTER OF SCIENCE

Approved by:

| | |
|---|---|
| Chair of Committee, | Mary Preston McDougall |
| Committee Members, | Steven M. Wright |
| | Chin B. Su |
| | Melissa A. Grunlan |
| Head of Department, | Costas Georghiades |

December 2008

Major Subject: Electrical Engineering

# ABSTRACT

RF Coil Design for Multi-Frequency Magnetic Resonance Imaging and Spectroscopy.

(December 2008)

Arash Dabirzadeh, B.Sc., Amirkabir University of Technology (Tehran Polytechnic)

Chair of Advisory Committee: Dr. Mary Preston McDougall

Magnetic Resonance Spectroscopy is known as a valuable diagnostic tool for physicians as well as a research tool for biochemists. In addition to hydrogen (which is the most abundant atom with nuclear magnetic resonance capability), other species (such as $^{31}P$ or $^{13}C$) are used as well, to obtain certain information such as metabolite concentrations in neural or muscular tissues. However, this requires nuclear magnetic resonance (NMR) transmitter/receivers (coils) capable of operating at multiple frequencies, while maintaining a good performance at each frequency. The objective of this work is to discuss various design approaches used for second-nuclei RF (radio frequency) coils, and to analyze the performance of a particular design, which includes using inductor-capacitor (LC) trap circuits on a $^{31}P$ coil. The method can be easily applied to other nuclei. The main advantage of this trapping method is the enabling design of second-nuclei coils that are insertable into standard proton coils, maintaining a near-optimum performance for both nuclei. This capability is particularly applicable as MRI field strengths increase and the use of specialized proton coils becomes more prevalent. A thorough performance analysis shows the benefit of this method over other

designs, which usually impose a significant signal-to-noise (SNR) sacrifice on one of the nuclei.

A methodology based on a modular coil configuration was implemented, which allowed for optimization of LC trap decoupling as well as performance analysis. The $^{31}P$ coil was used in conjunction with various standard $^{1}H$ coil configurations (surface/volume/array), using the trap design to overcome the coupling problem (degraded SNR performance) mentioned above. An analytical model was developed and guidelines on trap design were provided to help optimize sensitivity. The performance was analyzed with respect to the untrapped case, using RF bench measurements as well as data obtained from the NMR scanner. Insertability of this coil design was then verified by using it with general-purpose proton coils available. Phantoms were built to mimic the phosphorus content normally found in biologic tissues in order to verify applicability of this coil for in vivo studies. The contribution of this work lies in the quantification of general design parameters to enable “insertable” second-nuclei coils, in terms of the effects on SNR and resonance frequency of a given proton coil.

# ACKNOWLEDGEMENTS

I would like to thank all my teachers, professors, and mentors who have helped form my understanding of science and engineering throughout the years. Special thanks to all my committee members; my committee chair, Dr. Mary McDougall, who is an inspiration of hard work and maintaining high standards, Dr. Steve Wright, who has dedicated his knowledge and expertise to the business of saving lives. Thanks to the personnel of Philips Invivo Corp. especially Dr. Charles Saylor and Dr. Arne Reykowski. Also I would like to acknowledge my labmates, for their companionship during long days.

Thanks also go to all my friends for making the last couple of years a great experience. Last, but not the least, thanks to my parents who have dedicated their lives to culture and education and to my older brother whose never-ending support and encouragement got me where I am standing today.

# TABLE OF CONTENTS

CHAPTER Page

# LIST OF FIGURES

Page

Page

# LIST OF TABLES

# CHAPTER I

# INTRODUCTION

## I.1. NMR Spectroscopy

Nuclear magnetic resonance (NMR) spectroscopy has long been used in chemistry and more recently in molecular/metabolic medicine. With the increasing availability of whole-body high field-strength magnets for magnetic resonance imaging (MRI), non-proton spectroscopy is finding new promise as a diagnostic tool. Among nuclei with NMR capability, $^{13}C$ and $^{31}P$ have been of particular interest. $^{13}C$ found in organic compounds is used extensively in metabolic studies such as glucose labeling, and proton-decoupled magnetic resonance spectroscopy (MRS) of $^{31}P$ (which comprises 100% of phosphorus content), has diagnostic importance in ischemic cardiac myopathy[1] [2], a variety of brain disease[3], and also in monitoring effectiveness of cancer treatment procedures[4] [5]. Phosphorus metabolites, such as adenosine triphosphate (ATP) and phosphocreatine (PCr), are involved in reactions regulating energy delivery to the cells, as it is the equilibrium between the two that responds to a sudden rise in energy demand in muscular tissues. Advances in the design of spectrometers and MRI scanners are enabling in vivo interrogation of biological samples in animal and human studies.

---

This thesis follows the style of Journal of Magnetic Resonance.

## I.2. NMR Physics

Atoms with an odd number of protons or neutrons possess a magnetic moment. Nuclear Magnetic resonance makes use of this atomic property to extract signals containing information about materials present in the tissue. To do so, the sample is placed inside a strong static magnetic field ($B_0$). Atoms exhibit 2I+1 different energy levels given by equation (1)

$$E_m = -B_0 \gamma \bar{h} m \tag{1}$$

where $m = \pm I, \pm(I-1), \ldots$ , $\bar{h}$ = Planck's constant and $\gamma$ = Larmor ratio. The value of I for different nuclei is given in Table 1. An atom with I = ½ could have two distinct energy states, with the difference given by equation (2)

$$\Delta E = B_0 \gamma \bar{h} \tag{2}$$

In the absence of an external magnetic field, both states require the same amount of energy and are equally populated. Once an external $B_0$ is applied (along the z axis), atoms with a lower energy level slightly outnumber atoms with a higher energy level, causing a net magnetic moment along the direction of the applied external magnetic field (z). However, given enough energy, atoms can change states, causing the net magnetization vector to tip down from its equilibrium. Knowing the energy of a photon with angular frequency $\omega$ is given by equation (3) :

$$E = \bar{h}\omega \tag{3}$$

The frequency of a time-varying electromagnetic field required to cause the energy level transition is given by equation (4)

$$\omega = \gamma B_0 \tag{4}$$

where $\gamma$ is known as the Larmor frequency, which varies for different nuclei (Table 1).

Table 1 - NMR properties for some common nuclei

| Nucleus | I | Natural abundance % | $\gamma$(MHz/T) |
|---|---|---|---|
| $^{1}$H | ½ | 99.99 | 42.5759 |
| $^{2}$H | 1 | $1.5x10^{-2}$ | 6.5357 |
| $^{13}$C | ½ | 1.1 | 10.7054 |
| $^{14}$N | 1 | 99.6 | 3.0756 |
| $^{19}$F | ½ | 100 | 40.0541 |
| $^{23}$Na | 3/2 | 100 | 11.262 |
| $^{31}$P | ½ | 100 | 17.235 |

An RF magnetic field is applied perpendicular to the static field, tipping down the net magnetization vector towards the x-y (transverse) plane. Once the magnetization vector diverts from the z direction, a magnetic torque will be exerted on it, making it precess around the static magnetic field (z axis). The frequency of this precession is

known to be the same as Larmor frequency. Once the magnetization, or some portion of it, reaches the x-y plane, the RF field is cut off, allowing the magnetization to relax back to the z direction, releasing the RF energy that was just applied to it. The frequency of this RF signal is the same as the precession frequency, and the amplitude of this RF signal is proportional to the magnitude of the transverse portion of the magnetization vector.

NMR imaging uses space-varying static magnetic fields, known as gradient fields to frequency encode the spatial information into the resultant RF signal. Remember that the Larmor frequency is proportional to the static field $B_0$. So if we have a different magnetic field at each location, spins in different locations will precess at different frequencies. Because of the superposition principle, signals from different locations add up to the resultant RF signal, the frequency content of which corresponds to the extent of the sample. By taking the Fourier transform of this signal, we can find signal amplitude at each location, i.e. a projection image.

When this spatial localization is not implemented, the basic principle in use are those of NMR spectroscopy, used by chemists to identify unknown materials or concentration of certain compounds present in a sample. Different chemical compounds within the sample have slightly different $\gamma$ values than reference nuclei, (because of bonds to other atoms in the molecular structure), so they will precess at different frequencies. Frequency offset from the reference frequency is known as chemical shift, defined as:

$$\delta(ppm) = \frac{difference\ in\ precession\ frequency\ from\ a\ reference\ frequency(Hz)}{operating\ frequency\ of\ the\ magnet(MHz)}$$

The Fourier transform of the detected signal will give us the spectrum, showing peaks at certain frequencies. By mapping these to the table of chemical shifts, chemists can identify compounds present in the sample.

Molecular bonds not only change the Larmor frequency of the atom, they might also cause it to split into two frequencies; known as spin coupling. In this case, the resonance frequency of an atom will be dependent on the energy state of the neighboring, coupled atoms. This is especially true for bonds to hydrogen, in carbon and phosphorus compounds. Because of the low abundance of $^{13}C$ and phosphorus, splitting can further attenuate the signal, making it difficult to read. In order to overcome this problem, we need to "decouple" the hydrogen magnetization from our nuclei of interest (carbon or phosphorus). This is usually done via a saturation pulse. A high-power RF pulse at the hydrogen frequency is applied for a long time, usually on the order of 1 s, until the average hydrogen magnetization disappears. Then, the original signal of interest is read out. In this manner, hydrogen atoms will no longer affect carbon or phosphorus resonance frequencies.

### I.3. RF Coils

Transmission of an oscillating magnetic field, and detection of the resultant RF signal, is done via RF coils, or resonators. In transmit mode, a high-power RF amplifier is applied to the coil terminals, forming a current distribution on the coil conductors. This current generates a magnetic field ($B_1$) oscillating at the RF input frequency.

In receive mode, the magnetization vector within the sample is precessing, causing a flux change through the coil, inducing an electro-motive force (EMF) in the coil (Faraday induction). By amplifying this signal and taking the FFT, we have our spectrum.

Surface coils are the simplest form of RF coils used to produce/detect magnetic field. They usually provide better SNR than volume coils; since a smaller portion of the sample contributes to the received noise level; however the magnetic field inhomogeneity of surface coils can be a disadvantage.

The Biot-Savart law is commonly used as an analytical model to describe the magnetic field produced by an electric current. If we define a differential element of steady current (using the standard prime notation to mark the source variables) as $Id\boldsymbol{l}'$ and integrate over the current path, the vector magnetic potential [5] is found using equation (5) :

$$\boldsymbol{A}(\boldsymbol{r}) = \frac{\mu_0}{4\pi}\oint \frac{Id\boldsymbol{l}'}{r} \tag{5}$$

and the magnetic field will be

$$\boldsymbol{B}(\boldsymbol{r}) = \boldsymbol{\nabla} \times \boldsymbol{A}(\boldsymbol{r}) = \frac{\mu_0}{4\pi}\oint \frac{Id\boldsymbol{l}' \times \hat{\boldsymbol{r}}}{r^2} \tag{6}$$

where $\hat{\boldsymbol{r}}$ is the unit displacement vector between the current element (source) and the observation point, and $r$ is the distance between the two. The electric field can be found using equation (7)

$$\boldsymbol{E}(\boldsymbol{r}) = -\frac{\partial}{\partial t}\boldsymbol{A}(\boldsymbol{r}) - \boldsymbol{\nabla}\varphi \tag{7}$$

where $\varphi$ is the electric potential, contributing as a conservative electric field. Note that in this model (known as the quasi-static model), effect of the time-varying electric field on the magnetic field is ignored.

As an example, consider a loop of radius $R$ carrying stready current $I$ (Figure I-1),

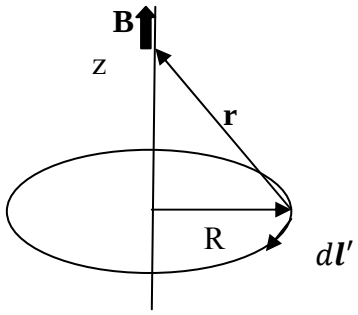


Figure I-1 - Magnetic field on the axis of a circular loop.

As we integrate $d\boldsymbol{l}'$ around the loop, $d\boldsymbol{B}$ sweeps out a cone. Horizontal components are cancelled, and vertical components add up to

$$B(z) = \frac{\mu_0 I}{4\pi}\int \frac{dl'}{r^2}\cos(\theta) \tag{8}$$

$$= \frac{\mu_0 I}{4\pi}\left(\frac{\cos(\theta)}{r^2}\right)2\pi R$$

$$= \frac{\mu_0 I}{2}\frac{R^2}{(R^2+z^2)^{\frac{3}{2}}}$$

on any point along the axis of the loop. Basically, any current-carrying conductor is capable of producing /detecting magnetic fields; however if it is operated at the resonance (minimum impedance) frequency, it will produce a much stronger field. Resonance is defined as the frequency at which imaginary components of the coil impedance cancel out, leaving purely resistive impedance (in a series model). By placing capacitors at one or more points along the coil, one can achieve resonance at any frequency of interest. Impedance of the coil (low-loss) can be modeled as:

$$Z = jL\omega + \frac{j}{C\omega} \tag{9}$$

where $L$ is the coil inductance and $C$ is the total capacitance used.

### I.4. Multi-frequency Applications and Motivation

Normally, to do phosphorus spectroscopy, using a single coil tuned to $^{31}$P is enough. However, there are several extremely common applications/motivations to justify the widespread usage of multiple-frequency excitation (typically proton excitation plus a second nucleus of interest). For example, the spin-coupling issue described in section I.2 can be mitigated using a technique called proton decoupling [6], which includes application of a high-power saturation RF pulse at the hydrogen frequency,

applied long enough for proton magnetization to disappear, thus removing its splitting effect on phosphorus resonances. For some molecules, phosphorus spectra are of little use unless protons are decoupled first. Figure I-2 shows a sample $^{31}P$ spectrum obtained from triphenyl phosphate, with and without proton decoupling. SNR(as measured by the peak height) before proton decoupling is very low.

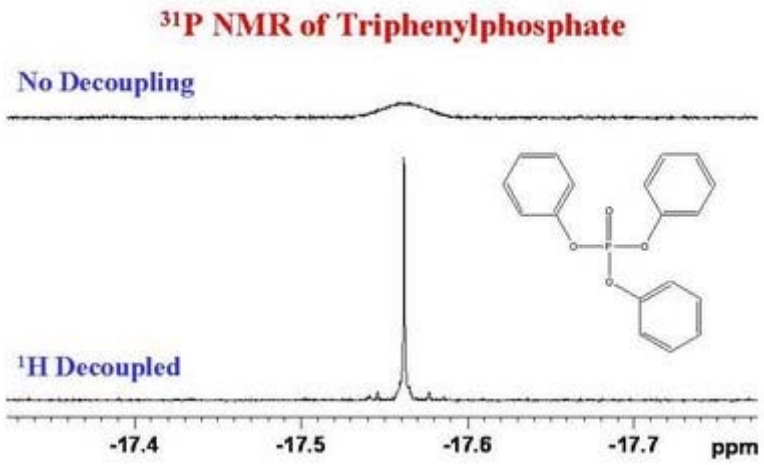


Figure I-2 – Effect of proton decoupling on phosphorus spectrum. Courtesy of University of Ottawa NMR facility.

In addition, in some applications, a $^{1}H$ scout image needs to be obtained in order to help with localizing second-nuclei spectra. Also, concurrent $^{1}H$ and $^{31}P$ spectra from the same area of interest are needed[4] for certain differential diagnosis.

NMR spectroscopy is also very sensitive to inhomogeneities in the static magnetic field, causing line-broadening in the spectra; so proper shimming is essential. However, the signal obtained from the observation nuclei ($^{31}P$ or $^{13}C$) is usually too

weak for shimming. A proton channel is therefore usually used to shim the static magnetic field in the region of interest.

In the case of low-abundant nuclei (such as $^{13}C$), a technique based on the Nuclear Overhauser Effect has been used to polarize proton spins and then transfer it to carbon spin population[7].

All of these applications require some way of exciting spins at two frequencies over the same region of interest.

## I.5. Multiple-frequency RF Coils

Because of this need for multi-frequency excitation (described in section I.4), it is worthwhile to examine the various possible design approaches for this task. In multi-nuclear applications, two nuclear species are interrogated; such as $^{1}H$ and $^{31}P$. The coil system needs to generate/detect RF magnetic field at two different frequencies; namely 200.23 MHz and 81.05 MHz for the case of $^{1}H$ and $^{31}P$ at 4.7 T. One method, a single-coil approach, uses inherently multiple-mode resonant structures.

Another method (chosen for implementation in this project) is to use two separate coils, each tuned to one frequency. Examples of the concentric or co-planar configurations are shown in Figure I-3.

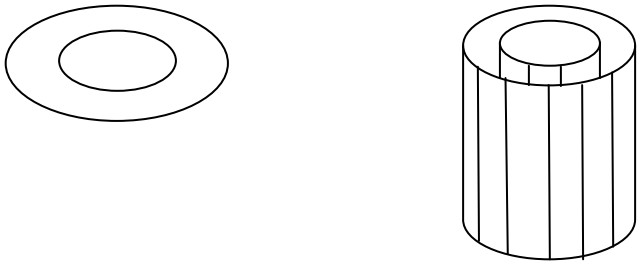

Figure I-3 – Two examples of concentric coil design. Left: surface coil Right: "birdcage" coil design.

The main problem with this approach is that flux generated by one coil links with the other one, inducing unwanted currents. A thorough review of previous work on dual-tuning is presented in chapter II.

## I.6. Importance of Insertability

Most of the previous approaches require designing coils for both frequencies for the dual-tuned system. However if there was a design that could enable using a stand-alone second-nucleus coil along with existing proton coils, it would save the cost of re-designing proton coils. In addition, as field strengths of whole-body magnets increase, proton coil designs are becoming increasingly specialized, usually entailing the use of complex multi-channel array coils that cannot easily be re-engineered for multi-frequency use. An "insertable" $^{31}$P coil is thus examined in this work, defined as not

affecting SNR and resonance frequency of a given $^{1}H$ coil; a methodology that can be straightforwardly applied to other nuclei of interest.

# CHAPTER II

# METHODS FOR DUAL-TUNING COILS

The growing demand for NMR spectroscopy along with a proton channel for localization, shimming, and proton decoupling, require dual-tuned MR probes that perform with high sensitivity. Even though optimal sensitivity cannot be achieved for both nuclei, some methods provide much better overall performance than others. In this chapter, the most common methods for dual-tuning are described.

## II.1. Single-Coil Approach

In this approach, the same conductor (resonant at two frequencies) is used for both nuclei.

### *II.1.1 Dual-tuning a Coil Using Lumped-element Traps*

One approach for dual-tuning a coil is using parallel LC traps in series with resonant elements[8]. Normally, in single-tuned coils (Figure II-1), a capacitor is used in series[1] with coil inductance to cancel-out the reactive impedance (series model is normally used [9] to study dual-tuned resonance behavior and SNR)

[1]A series LC circuit resonates (zero impedance) at the same frequency as it would as a parallel resonator (infinite impedance). Matching/tuning strategy is merely a matter of transmission line characteristic impedance or the impedance required to noise-match a preamplifier and does not affect coil SNR and resonance frequency.

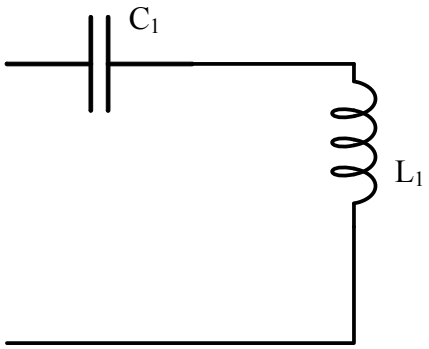


Figure II-1 – Impedance model for a RF coil.

$$\frac{1}{C_1\omega} = L_1\omega \tag{10}$$

In this model, resonance is achieved at a single frequency. Now if we add a parallel LC to the above configuration (Figure II-2), the resonance equation becomes the following[9]:

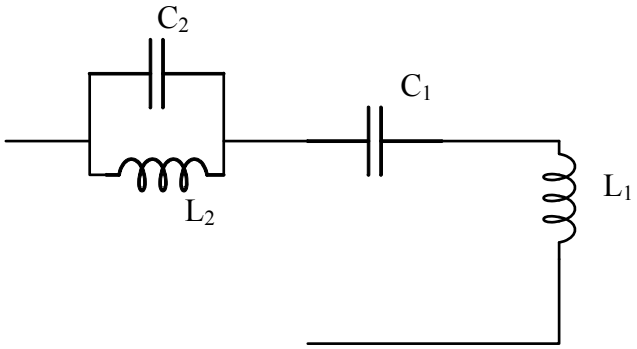


Figure II-2 – Resonance model for a dual-tuned coil

$$\frac{L_2\omega}{1 - C_2L_2\omega^2} - \frac{1}{C_1\omega} + L_1\omega = 0 \tag{11}$$

Or

$$L_2\omega\frac{1}{1-\frac{\omega^2}{{\omega_2}^2}}+\frac{1}{C_1\omega}\left(\frac{\omega^2}{{\omega_1}^2}-1\right)=0 \tag{12}$$

where $\omega_1$ is the resonant frequency of the single-tuned coil and $\omega_2$ is the resonance frequency of the trap.

There will be two frequencies (two modes) that satisfy the above equation and can be used to operate the coil at minimum impedance required for effective transmission and reception. Figure II-3 shows the reactance of a single-tuned coil (dashed line) along with a parallel LC trap, generated using equation (12). Putting the two in series will introduce two new resonant modes, corresponding to the intersections of two graphs. Note that the trap has positive reactance at the lower frequency (equivalent to an inductor) and negative reactance at the higher frequency (equivalent to a capacitor). The lower mode will be close to the single-tuned coil resonance (thus mostly governed by $C_1$), and the higher mode will be close to the trap resonance (thus mostly governed by $C_2$ and $L_2$).

At the higher-frequency mode, the current in the trap inductance is out-of-phase with the current in the coil inductance; while at the lower-frequency mode, the current in both inductors are in-phase.

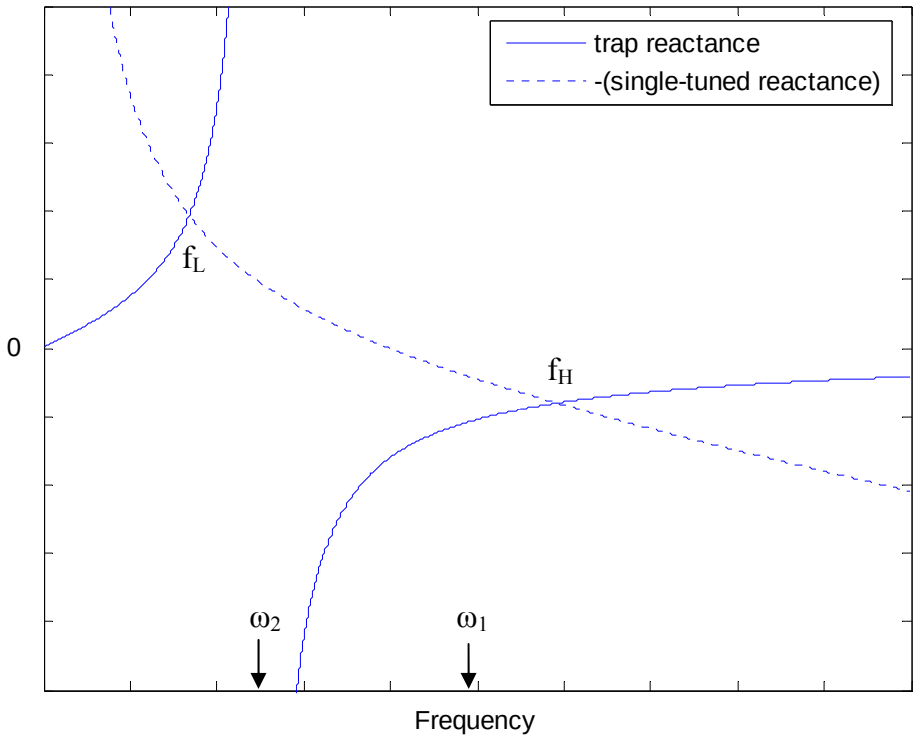


Figure II-3 – Reactance of a single-tuned coil and a trap. The two intersections mark the two resonant modes of the trap in series with the coil.

The efficiency of this coil at the two frequencies might not be equal. Defining the efficiency as the ratio of the power delivered to the load to the power dissipated in the trap, it is shown[8] that at the higher frequency:

$$E = \left(\frac{L_2}{L_1 + L_2}\right)^{1/2} \tag{13}$$

while at the lower frequency:

$$E = \left(\frac{L_1}{L_1 + L_2}\right)^{1/2} \tag{14}$$

At the higher frequency, we are operating close to the resonance mode of the trap circuit; so a large trap inductance causes a higher circulating current in the tank circuit, and higher noise contribution. So in order to minimize the effective trap loss at the higher frequency, trap inductance needs to be chosen to be relatively higher than coil inductance; while at the lower frequency (which is usually more critical because of low-abundance nuclei) we are operating far lower than the trap resonance, so the current running in the trap inductance $L_2$ is approximately equal to the current running in the coil inductance $L_1$; so the effective trap loss will be proportional to the trap inductance (assuming a fixed inductor Q). So it is necessary to choose $L_2$ to be small compared to $L_1$. This tends to be one of the main disadvantages of the single-coil design, since a major compromise needs to be made: if the design is optimized for the lower-frequency nuclei, proton performance will be typically reduced by half [8].

In order to use this coil, impedance needs to be matched to 50 ohms. Dual-tuned coils can have either a single input, where both modes are excited through a single port, or two inputs. In sequential applications where simultaneous operation of the two modes is not required, a single input coil can be used, along with a single-channel RF amplifier. However in applications where two modes are operated at the same time (such as proton decoupling), two separate inputs to the coil are required.

Transformer-drive excitation is usually used to couple into this scheme of dual-tuned coils, especially for single-input cases; since the matching schemes used with transformer coupling [10; 11] tend to be independent of frequency; so the same matching strategy can be used for both frequencies. In a direct excitation (using a cable across a tuning element) it requires a matching reactance (dependent on the probe inductance and Q) that will be different for two frequencies; so we actually need a trap circuit, to provide two different matching reactances at the two operation frequencies. A single-input design based on [8] is given in Figure II-4

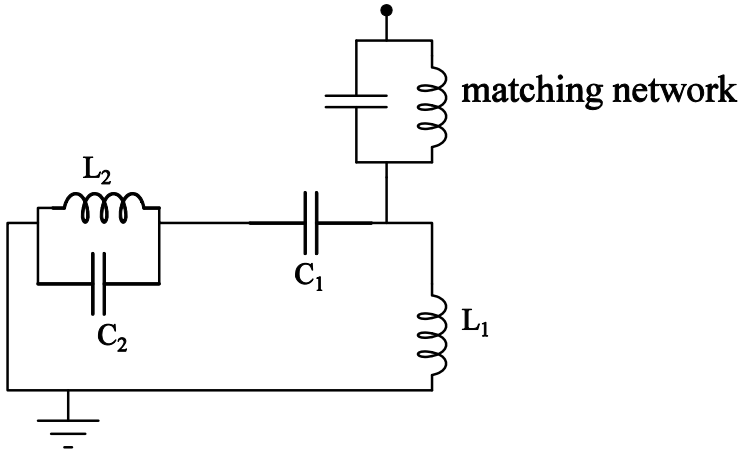


Figure II-4 – Single-input dual-tuned coil.

A dual-input scheme first suggested in [12] is shown in Figure II-5; in which two modes are excited through separate inputs and matching networks; however isolation between the two ports tends to be a problem.

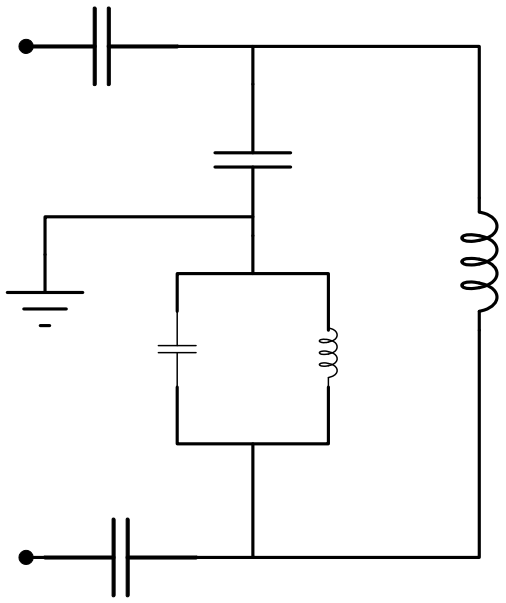

Figure II-5 – Dual-tuned single-coil with two input ports.

Volume coil embodiments using the single-coil design can be found in [13], [14]

### *II.1.2 Dual-tuning a Coil Using Isolation Filters*

Another scheme, first introduced in [15; 16], is shown in Figure II-6 . Quarter-wavelength transmission line segments are used to isolate the high-frequency and low-frequency ports. In the original design [15], variable-length transmission lines were also used for tuning instead of capacitors.

The theory behind this method is based on standard transmission line theory: A loss-less transmission line of length $l$ and characteristic impedance $Z_0$ can be used as an impedance transformer:

$$Z_{in}(l) = Z_0 \frac{Z_L \cos(\beta l) + Z_0 j sin(\beta l)}{Z_0 \cos(\beta l) + Z_L j sin(\beta l)} \tag{15}$$

where $\beta$ is the propagation constant equal to $2\pi/\lambda$ . With $l = \lambda/4$:

$$Z_{in}\left(\frac{\lambda}{4}\right) = \frac{{Z_0}^2}{Z_L} \tag{16}$$

Therefore, An open-circuited quarter-wavelength ($Z_L = \infty$) will look like a short circuit, and a short-circuited quarter-wavelength will look like an open circuit.

In Figure II-6, it can be seen that at the high frequency, the open-circuited line on the left will look like a short circuit, blocking the high-frequency signal from getting into the low-frequency part; while the short-circuited line on the right will look like an open circuit, leaving the high-frequency signal unaffected.

The reason that line segments are designed at the high-frequency nuclei is that in proton decoupling, the proton coil (high frequency) is transmitting large amounts of power into the coil while the observation nuclei(low-frequency circuit) is receiving; so it is crucial to isolate the high-power proton signal from low-frequency circuitry and preamplifiers.

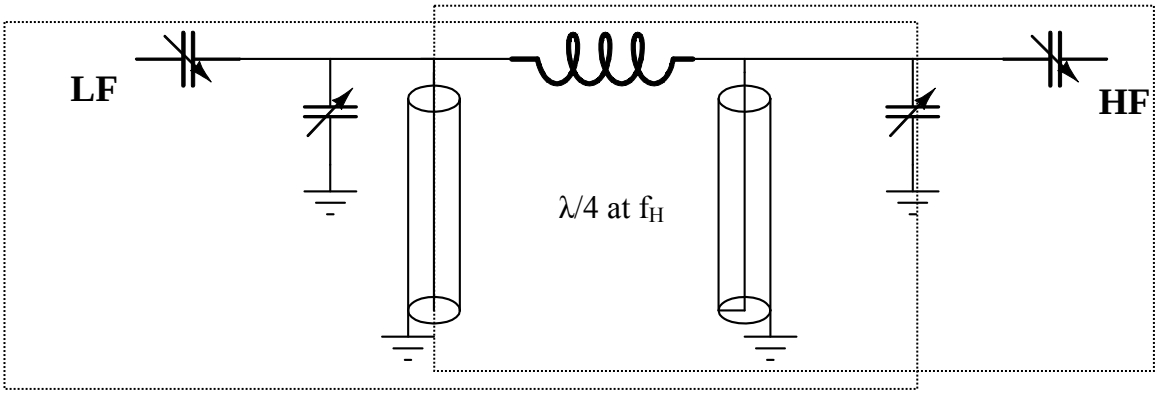


Figure II-6 – Dual-tuned single coil with two isolated inputs.

In a special case, where the lower-frequency nucleus is $^{13}C$, we will have perfect isolation for both frequencies. The gyro-magnetic ratio of $^{13}C$ happens to be four times that of $^{1}H$; so a quarter-wavelength line at the $^{13}C$ frequency is a full-wavelength line at hydrogen frequency. By using a shorted quarter-wavelength line at the left side and open quarter-wavelength line at the right (Figure II-7), the LF signal will see an open at point A and will continue unaffected; after passing through the coil, it will see a short-circuit to the ground at point B, isolated from the HF side. The HF signal sees an open at point B, continuing into the coil unaffected. At the point A it will see a short-circuit to the ground, being isolated from the LF side.

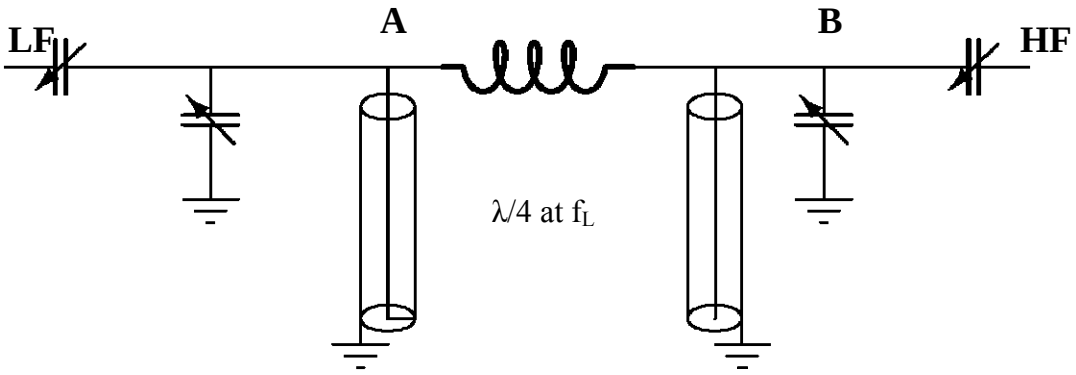


Figure II-7 - Dual-tuned single coil for $^{13}C$ and $^{1}H$.

Lumped-element equivalents are suggested in [17] for an isolating filter which is open at a desired frequency and short at a second one, generalizing this perfect isolation to other nuclei pairs. The circuit in Figure II-8 (a), can act as an open at the higher frequency and as a short at the lower frequency, so it is suitable for the HF side of the dual-tuned coil (such as hydrogen). The design formulas are[17]:

$$\omega_{LF} = \frac{1}{\sqrt{LC_1}} \tag{17}$$

$$\omega_{HF} = \frac{1}{\sqrt{\frac{C_1 + C_2}{C_1 C_2 L}}} \tag{18}$$

The circuit in Figure II-8 (b), can act as an open at the lower frequency and as a short at the higher frequency, so it is suitable for the LF side of the dual-tuned coil(such as carbon or phosphorus). The design formulas are[17]:

$$\omega_{LF} = \frac{1}{\sqrt{LC_1}} \tag{19}$$

$$\omega_{HF} = \frac{1}{\sqrt{\frac{(L_1 + L_2)C_1}{L_1 L_2}}} \tag{20}$$

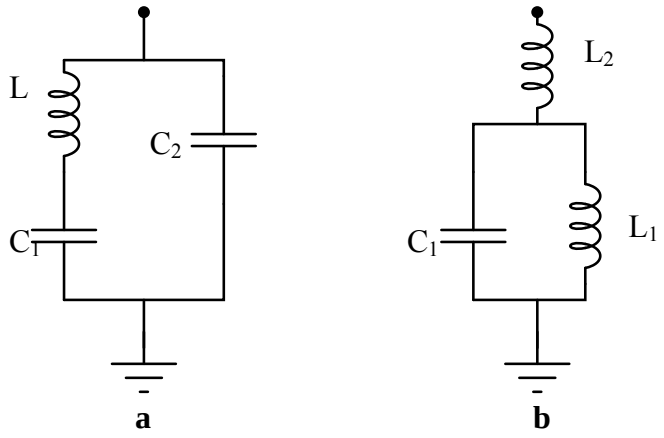


Figure II-8 – Lumped-element shunt isolation filters. (a): used at the HF side (b): used at the LF side.

Doty et al [18] presented a lumped-element version of this scheme, where quarter-wavelength segments are replaced by lumped element(capacitor-inductor)

equivalents for better efficiency. It is shown that by changing the ratio of the coil inductor to the filter inductor, one can adjust the efficiency of the system and reach the desired compromise between LF and HF efficiency, as well as a wide tuning range for each.

## II.2. Dual Coil Approach

While dual-tuned single coils(described in the previous section) have been used in the past (especially in chemistry, where coils are small compared to the wavelength), it is usually more advantageous to separate the two modes into two coils. With this approach, each coil can be individually optimized for the application, and isolation between the two is easier to achieve. Also, if using a phosphorus coil with existing proton coils is desired, a two-coil design is obviously the method of choice.

Whenever two coils are placed in proximity of each other, the magnetic flux generated by one is linked to the other coil(unless they are orthogonal to each other). Using Faraday's induction law for a RF magnetic field linked to a coil of surface $\Sigma$ :

$$EMF = -j\omega \iint_{\Sigma} \boldsymbol{B} \cdot d\boldsymbol{A} \tag{21}$$

This EMF produces an induced current on the second coil, which can be modeled as a circuit with mutual inductance (Figure II-9).

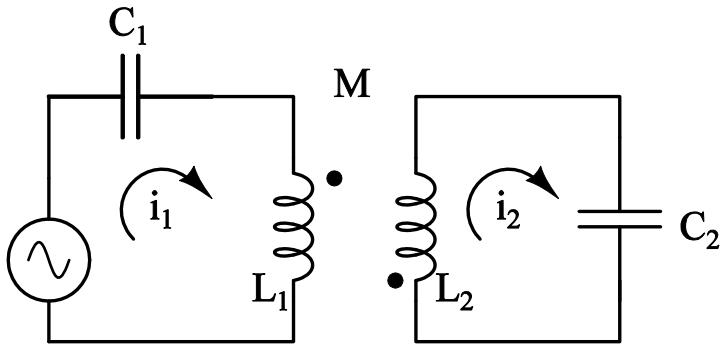


Figure II-9 – Equivalent circuit for two loss-less coupled coils.

Using Kirchoff's Voltage Law (KVL) for the two meshes and assuming a self-inductance of $Z_s$:

$$E = i_1(Z_s + jX_{C1} + jX_{L1}) + i_2 jX_M$$

$$0 = i_1 jX_M + i_2 j(X_{C2} + X_{L2})$$

solving for $i_2$ :

$$i_2 = \frac{-jX_M i_1}{j(X_{C2} + X_{L2})} \tag{22}$$

with $X_M$ being the inductive mutual reactance which is dependent on distance/orientation of coils to each other. Consider two cases:

*Second coil having inductive impedance*

In this case, $X_{C2} + X_{L2}$ will be positive, and using equation (22): $i_2 = -\left|\frac{X_M}{X_{C2}+X_{L2}}\right| i_1$, i.e. current induced in the second coil will be 180 degrees *out of phase* with the excitation current in the main coil.

*Second coil having capacitive impedance*

In this case, $X_2$ will be negative, and using equation (22): $i_2 = \left|\frac{X_M}{X_{C2}+X_{L2}}\right| i_1$, i.e. current induced in the second coil will be *in phase* with the excitation current in the main coil.

A series LC resonator operated *above* its resonance frequency will have inductive reactance; thus supporting an induced current counter-rotating from the excitation current. Similarly, a resonator operated *below* its resonance frequency will have capacitive reactance supporting an induced current co-rotating with the excitation current.

Therefore, when we are operating the system at the hydrogen frequency, the phosphorus coil will act as an inductor; while at the phosphorus frequency, hydrogen coil will act as a capacitor. Fitzsimmons et al. [19; 20] showed this phenomenon by PSpice™ simulation of current phase responses. Depending on orientation of the two

coils to each other, the counter-rotating currents can cause significant loss in magnetic field intensity.

Geometric decoupling is one method used in the past to fix this problem of counter-productive current generation. If we can produce a proton magnetic field perfectly parallel to the phosphorus coil plane, there will be no flux linked with the phosphorus coil, and there will be no induced currents. A figure-8 shaped, or butterfly coil[21] (shown in Figure II-10-b) provides a magnetic field parallel to the coil plane (in the middle), significantly reducing the coupling to the normal $^{31}P$ field. Another design, known as co-planar dual-loop surface coil[22], consists of a center-fed loop, producing counter-rotating currents in the half-loops, which will create a magnetic field parallel to the plane. (Figure II-10-a)

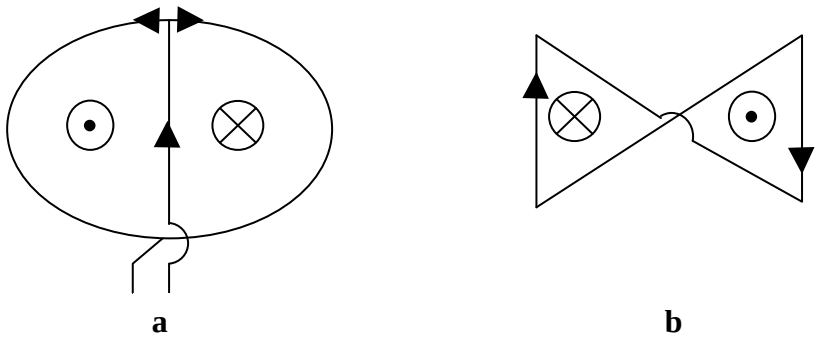


Figure II-10 – Two coil designs producing a magnetic field parallel to their plane. Current and magnetic field directions are shown. At the middle of the coil, magnetic field is parallel to the plane. (a) Butterfly or figure-8 coil design and (b) co-planar dual loop design.

Although these designs provide good decoupling between the proton coil and phosphorus coil, the parallel magnetic field intensity produced by the proton coil tends to fall off very quickly as we move away from the coil plane; so if the region of interest

is located at deeper distances, this design will not provide sufficient proton performance. A more recent design [23] is shown in Figure II-11. Two proton surface coils are wrapped around a half-cylinder formation, to produce orthogonal magnetic field in the center. Using the fact that the magnetization in the material is also circularly polarized, this method provides a significant gain compared to a linearly-polarized magnetic field.

If the two coils are fed with a signal and its 90 degree phased-shifted version, it will produce a RF magnetic field with circular polarization. Effective transverse coil sensitivity is defined as:

$$B_{1t} = \boldsymbol{B}_{coil} \cdot \boldsymbol{p}_M \tag{23}$$

where $\boldsymbol{p}_M = \frac{1}{\sqrt{2}}(\boldsymbol{a_x} + j\boldsymbol{a_y})$. For a linearly-polarized coil:

$$B_{t,linear} = |\boldsymbol{B}|\boldsymbol{a_x} \cdot \frac{1}{\sqrt{2}}(\boldsymbol{a_x} + j\boldsymbol{a_y}) = \frac{1}{\sqrt{2}}|\boldsymbol{B}| \tag{24}$$

If we use a 3 dB, 90 degree phase-shift power divider (known as a quadrature hybrid combiner) to divide the power by 2 (divide the field magnitude by $\sqrt{2}$) and feed the in-phase signal to one coil and quadrature-phase signal to the orthogonal coil, it will produce a circularly-polarized field

$$B_{t,circular} = |\boldsymbol{B}|\left(\frac{1}{\sqrt{2}}\boldsymbol{a_x} - \frac{1}{\sqrt{2}}j\boldsymbol{a_y}\right) \cdot \frac{1}{\sqrt{2}}(\boldsymbol{a_x} + j\boldsymbol{a_y}) = |\boldsymbol{B}| \tag{25}$$

which is equivalent to a sensitivity gain by a factor of $\sqrt{2}$ and transmitted power gain by a factor of 2.

By placing the lower-frequency coil at a distance from the protons, the blocking field problem is reportedly [23] solved (as shown in Figure II-11 ), providing -20 dB isolation between the $^{31}C$ coil and $^{1}H$ coils. Isolation between two quadrature proton coils is achieved by overlapping the two, providing a shared flux area that cancels out the direct flux linkage between the two.

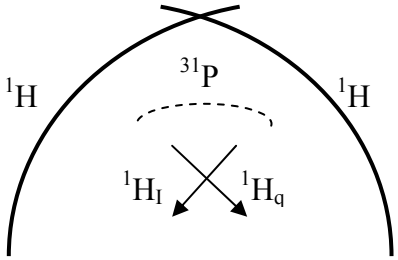


Figure II-11 – Half-volume quadrature dual-tuned coil design.

This chapter has reviewed the basic design options for dual-frequency NMR excitation coils. An emphasis has been placed on dual-coil design methods, as this provides a direct route towards developing "insertability" capabilities for second nuclei coils. The following chapter presents the primary design consideration to enable this insertability.

# CHAPTER III

# USING TRAPS IN DUAL-COIL DESIGN

Various design approaches to the dual-tuning problem were discussed in the previous chapter. A particular design, using a trap circuit tuned to the $^{1}H$ frequency on the $^{31}P$ coil was chosen, implemented, and thoroughly analyzed in this project, using bench measurements as well as imaging/spectroscopy tests. An analytical model is developed and guidelines on trap design are provided to help optimize performance. The main advantage of this method is enabling the design of second-nuclei coils that are insertable into standard proton coils, maintaining a near-optimum performance for both nuclei.

## III.1. Tank Circuits

LC traps are tank circuits composed of an inductor and capacitor in parallel, providing very high impedance at the tank resonance frequency. The first example of usage in NMR coils appears in [24], where a trap is used as an external filter, along the dual-tuned receiver chain, in order to isolate the two frequencies in a dual-tuned TEM (transverse electromagnetic) coil.

Ideal traps have no loss; and provide infinite impedance at their resonance. Unfortunately inductors have a resistance associated with them(typical inductor Q is below 300, while for capacitors it is usually above 1000); thus particularly limiting performance. A model of this non-ideal trap circuit is diagrammed in Figure III-1.

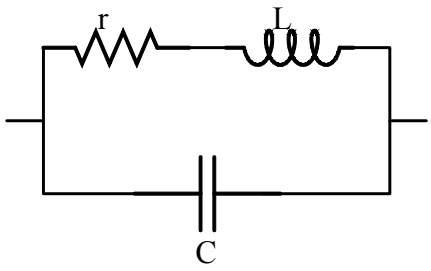


Figure III-1 – Non-ideal LC trap circuit.

According to this model, the trap has impedance

$$Z = \frac{(jL\omega + r)\left(\frac{-j}{C\omega}\right)}{jL\omega + r - \frac{j}{C\omega}} = \frac{L\omega - jr}{jLC\omega^2 + rC\omega - j} \tag{26}$$

at resonance:

$$Z = \frac{L\omega_0 - jr}{rC\omega_0} = \frac{1 - \frac{jr}{L\omega_0}}{\frac{rC}{L}} \tag{27}$$

using the approximation $\frac{r}{L\omega} \ll 1$,

$$Z = \frac{L}{rC} = \frac{L^2{\omega_0}^2}{r} = Q\omega_0 L \tag{28}$$

where $Q$ is the quality factor of the inductor used, defined as $Q = \frac{\omega_0 L}{r}$. The real and imaginary parts of the trap impedance are plotted in Figure III-2, generated using equation (26) .

It follows that using high-Q inductors is desired in order to achieve a high blocking impedance.

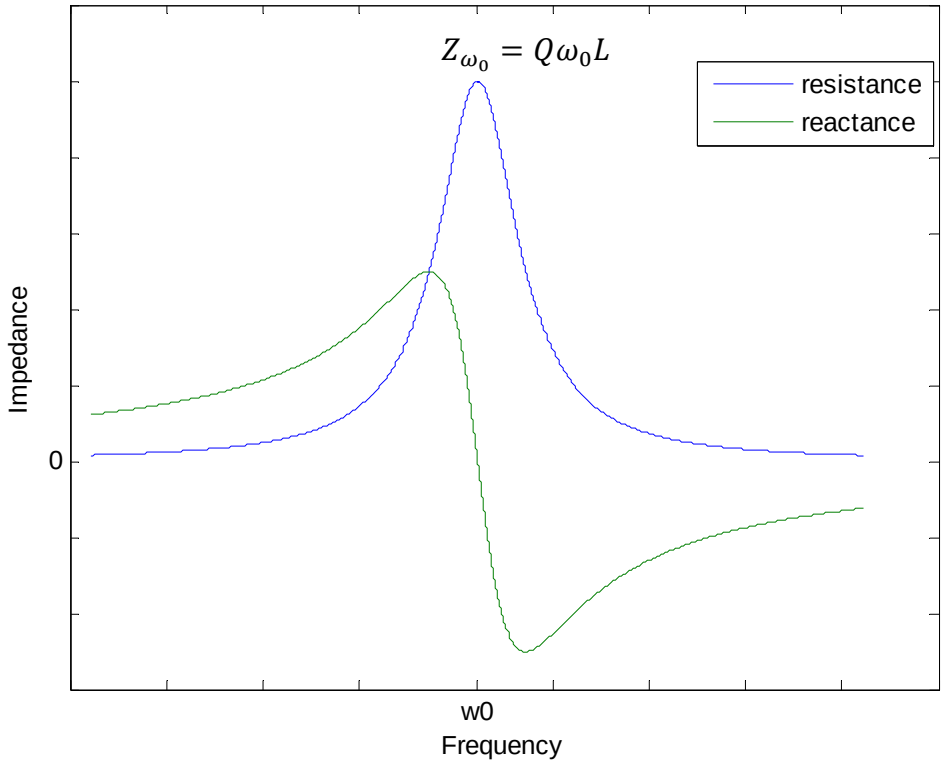


Figure III-2 – Real and imaginary parts of non-ideal trap impedance.

## III.2. Coil Implementation

Surface coils are commonly used when high signal-to-noise is required at a depth close to the surface. We implemented a concentric design, consisting of an outer coil for proton and inner coil for phosphorus. Coils can be fabricated on a single PC board,

however we will show later that a modular, separable design is essential for optimization of the trap as well as application flexibility (potential of having a stand-alone $^{31}P$ coil, insertable into proton coils). Two loops were cut(12.44 cm and 7.1 cm diameter, 1 cm wide) from a FR-4 PCB (which is known to provide good Q) using in-house protoboard machine (LPKF C30, Wilsonville, OR). In anticipation of high-field surface coil design, a shield was included to limit radiation loss. The coil configuration is shown in Figure III-3.

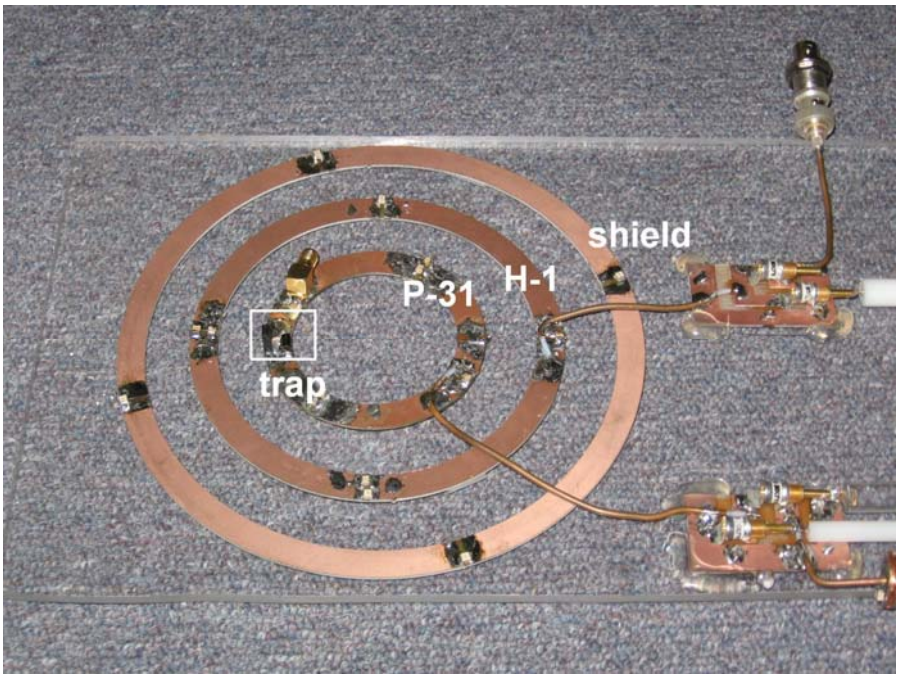


Figure III-3 – Concentric surface coil structure.

In a standard surface coil fashion, four equally spaced gaps were cut to place tuning elements and ensure in-phase current at different locations along the loop, despite the high operation frequency. Resonance was achieved by placing surface-mount

capacitors (American Technical Ceramics, Huntington Station, NY) across the gaps. Matching capacitors are placed somewhere down the cable. Theoretically, matching networks can be placed anywhere between the generator and load on a transmission line; however since we prefer to use capacitive matching rather than inductive, it is important that cable length between the coil and the matching network is either half-wavelength (which presents the same inductance as we would see across coil input port) or a length that preserves inductive reactance, which can be zeroed-out by a matching capacitor. (For example, a length of quarter-wavelength would transfer the coil inductance to a capacitance, which requires inductive matching). Table 2 presents the capacitor values used to tune each coil.

Table 2 - Resonance frequency and distributed capacitor values used in each coil

| coil | Resonance frequency(MHz) | Capacitor values(pF) |
|---|---|---|
| Hydrogen | 200.228 | 6.8 |
| phosphorus | 81.05 | 115 |

### III.3. Coupling Effects

Each coil was individually tuned and matched, and then placed together in a concentric fashion. An important point is the shift in resonance frequency of each coil, especially proton coil. To find the resonance frequencies of coupled coils, two cases are considered, where the coils are initially tuned to the same frequency (degenarate) or to separate frequencies.

*III.3.1 Initially Tuned Degenerate*

Again, as was used in section II.2, a circuit model of two coupled coils is shown in Figure III-4.

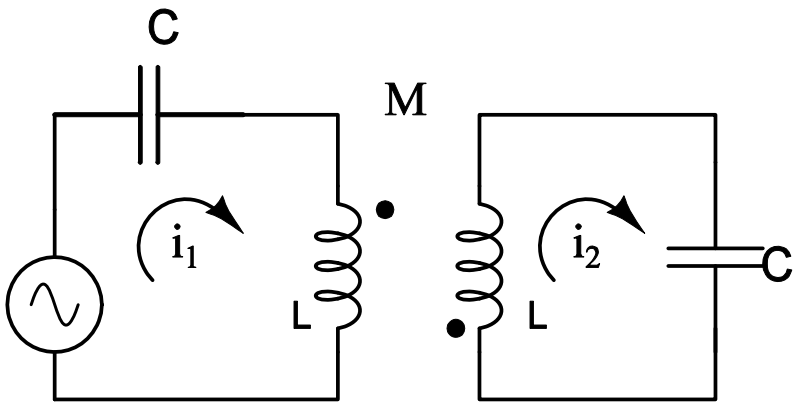


Figure III-4 –Equivalent circuit diagram of two degenerate coils placed near each other.

Using KVL as before

$$E = i_1 j(X_L - X_C) + i_2 j X_M$$

$$0 = i_1 j X_M + i_2 j(X_L - X_C)$$

Where the mutual inductance $X_M = kX_L$.

To find the resonance frequency, first we find the impedance:

$$Z = \frac{E}{i_1} = j(X_L - X_C) - j\frac{k^2 {X_L}^2}{X_L - X_C} \tag{29}$$

At resonance, the reactive impedance is zero:

$$(X_L - X_C)^2 = k^2 {X_L}^2 \tag{30}$$

After expansion and division by ${X_C}^2$:

$$1 - 2\frac{X_L}{X_C} = (k^2 - 1)\left(\frac{X_L}{X_C}\right)^2 \tag{31}$$

Knowing that coils are individually tuned to $\omega_0$ :

$$\frac{X_L}{X_C} = LC\omega^2 = \frac{\omega^2}{{\omega_0}^2}$$

Substituting into (31):

$$1 - 2\left(\frac{\omega}{\omega_0}\right)^2 + (1 - k^2)\left(\frac{\omega}{\omega_0}\right)^4 = 0$$

$$\left(\frac{\omega}{\omega_0}\right)^2 = \frac{1 \pm \sqrt{1 - (1 - k^2)}}{(1 - k^2)} = \frac{1}{1 \pm k} \tag{32}$$

Knowing that $k \leq 1$ , it is shown that coupling causes the resonance frequency to split apart into two frequencies.

### *III.3.2 Initially Tuned to Separate Frequencies*

This is the case with multi-nuclear coils; since each one is tuned to the nucleus of interest. Equation (30) becomes

$$\left(X_{L_1} - X_{C_1}\right)\left(X_{L_2} - X_{C_2}\right) = k^2 X_{L_1} X_{L_2}$$

After expansion and division by $X_{C_1} X_{C_2}$ :

$$1 - \frac{X_{L_2}}{X_{C_2}} - \frac{X_{L_1}}{X_{C_1}} = (k^2 - 1)\frac{X_{L_1}}{X_{C_1}} \cdot \frac{X_{L_2}}{X_{C_2}} \tag{33}$$

Knowing the fact that coil 1 is tuned to $\omega_1$ and coil 2 is tuned to $\omega_2$:

$$\frac{X_{L_1}}{X_{C_1}} = L_1 C_1 \omega^2 = \frac{\omega^2}{{\omega_1}^2} \quad , \quad \frac{X_{L_2}}{X_{C_2}} = L_2 C_2 \omega^2 = \frac{\omega^2}{{\omega_2}^2}$$

Substituting into (33) :

$$1 - \left(\frac{\omega}{\omega_2}\right)^2 - \left(\frac{\omega}{\omega_1}\right)^2 + (1 - k^2)\left(\frac{\omega^4}{{\omega_1}^2 {\omega_2}^2}\right) = 0 \tag{34}$$

which can be numerically solved to predict the shifted resonance frequencies as a result of coupling. The predicted resonance shifts (in MHz) for both coils ($^{1}$H and $^{31}$P) operating at 4.7T are shown in Figure III-5. A different form of equation (34) is presented in [20]

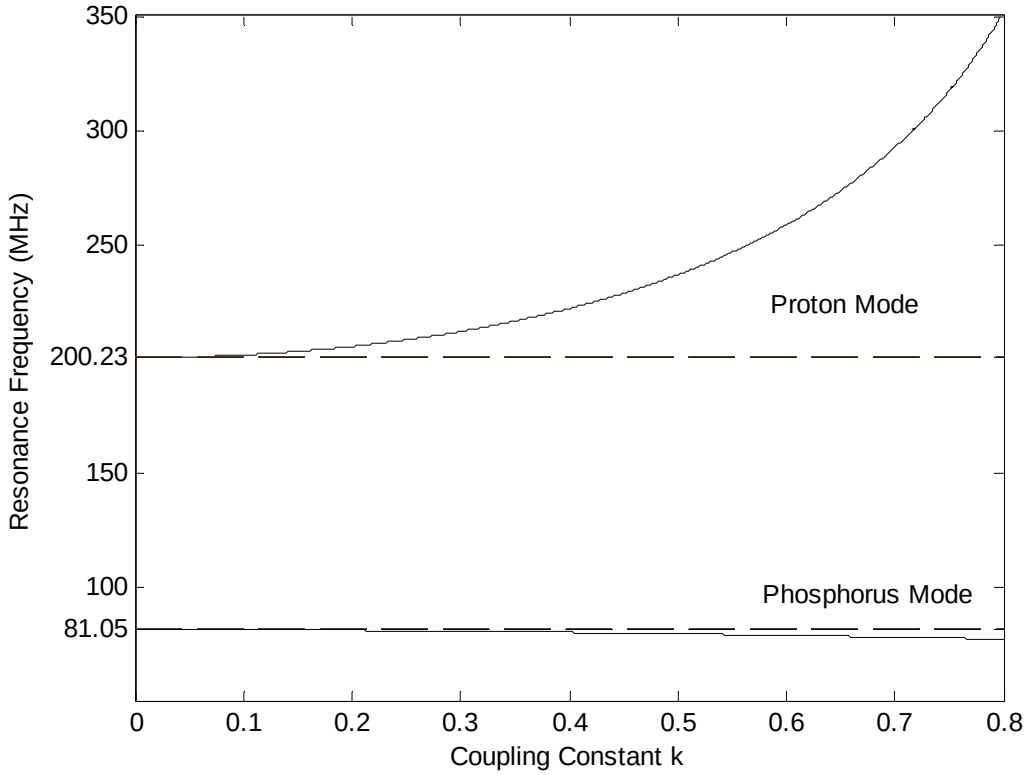


Figure III-5 – Effect of coil coupling between $^{1}H$ coil and $^{31}P$ coil at 4.7T, manifesting itself as a shift in the desired resonance frequency.

## III.4. Bench Measurement Results

In case of our concentric coils, coupling caused the proton resonance frequency to move up to 208 MHz and phosphorus resonance frequency down to 80.05MHz. Figure III-6 depicts a screenshot from Agilent 5071 network analyzer showing this resonant shift.

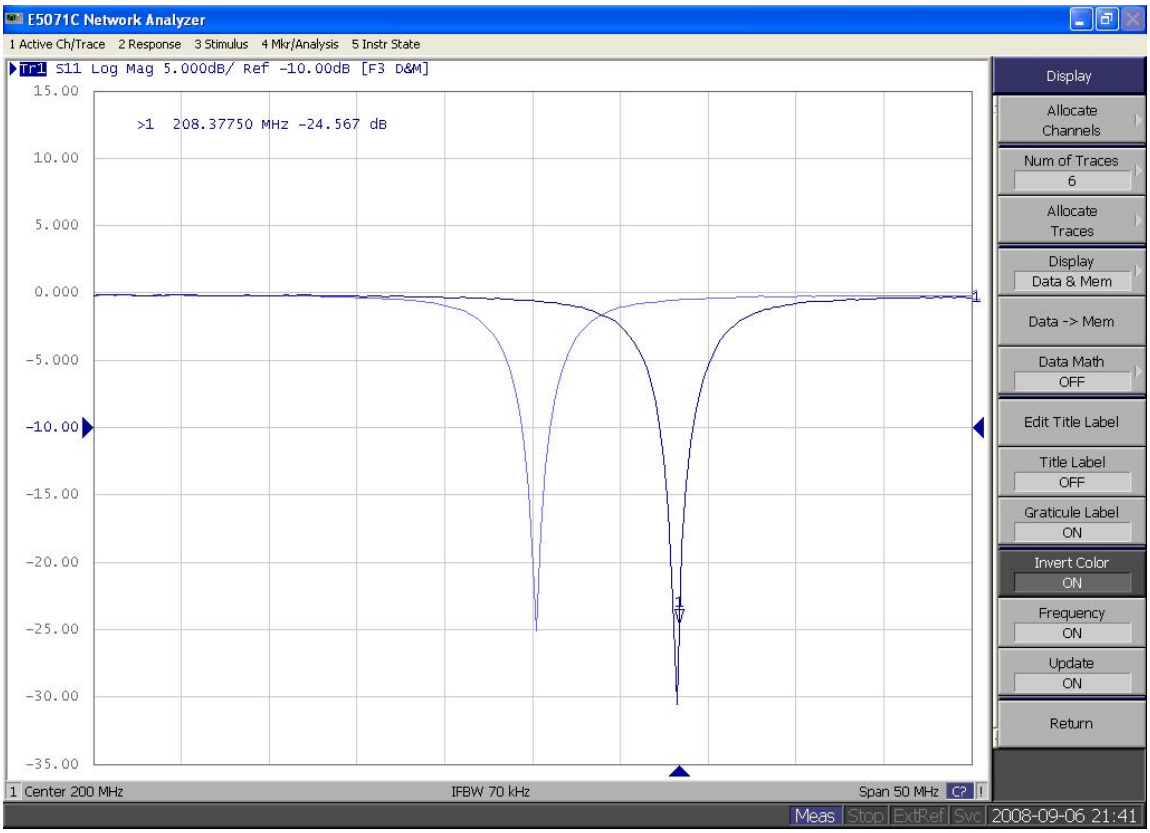


Figure III-6 – Screenshot from Agilent 5071 network analyzer showing the effect of the $^{31}P$ coil on $^{1}H$ resonance frequency(shift of 8 MHz).

Causing a significant shift in the resonance frequency of the proton coil is one of the reasons that a phosphorus coil cannot simply be inserted into existing proton coils. Depending on coupling between the two coils, this shift in proton coil tuning can vary (for two same-size coils of 2" diameter, the proton resonance shift is about 50MHz).

Another, perhaps more important effect of adding the phosphorus coil is a change (degradation) in the magnetic field intensity of the proton coil. As discussed in section II.2, at the proton frequency, the phosphorus coil supports strong, out-of-phase current

that effectively blocks the magnetic field produced by the proton coil in the center. This effect is shown in Figure III-7. The standard method to estimate field intensity and SNR of a coil is to excite a matched coil using a cable and receive the signal by a field probe (known as "pick-up loop"). Using a network analyzer, this can be done using an $S_{21}$ measurement. It is important to maintain the tune/match when using this method to compare different coils. One can also use a loop (dual pick-up loop consists of two decoupled small loops, one for excitation and one for detection. It is also used to find resonance frequency and Q of a resonator) in order to inductively excite the coil instead of using a 50 ohm cable; making the measurement less prone to change in matching conditions. In Figure III-7, the magnetic field is measured on the axis, at 2.5 cm (1/3 coil width) above the coil surface. The top curve is for the proton coil alone, and the bottom curve is after putting on the phosphorus coil and retuning/rematching. 4.7 dB loss in the on-axis magnetic field intensity is observed, corresponding to about 45% loss in magnetic field intensity generated by the proton coil.

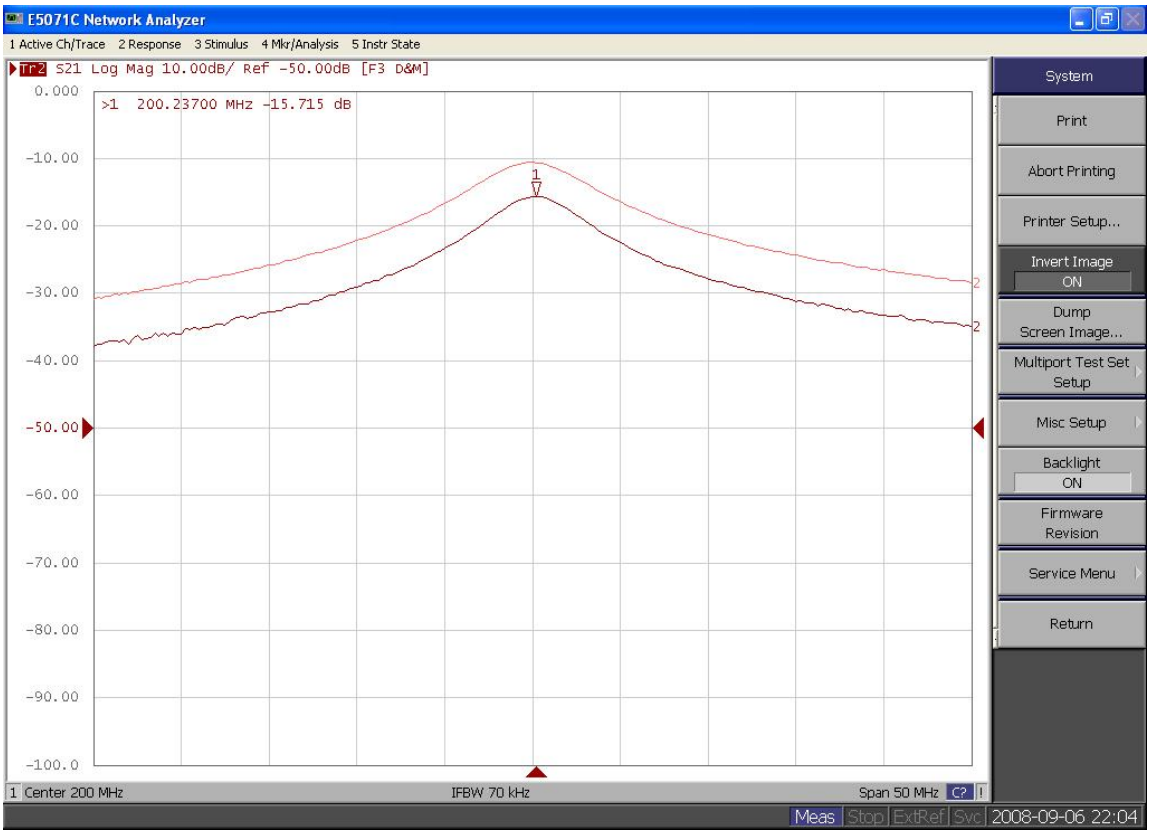


Figure III-7 – Effect of $^{31}$P coil on $^{1}$H field intensity. $^{1}$H coil alone (top) , $^{31}$P coil present (bottom).

The Principle of Reciprocity states that the voltage produced from the location of interest induced in a receiving coil is proportional to the magnetic field intensity that would be produced at that location if a 1 Amp current was running in the coil. In other words, antennas work equally well as transmitters or receivers. A 45% loss in transmission is equivalent to 45% loss in received SNR.

Knowing that these two problems (shift in resonance frequency and SNR) are caused by the coupled currents in the phosphorus coil, we know that if we can somehow make the phosphorus coil appear open at the proton frequency, we can eliminate this

current. Alecci et al[25] used LC traps, tuned to proton frequency, on their Na coil. In order to tune this trap properly, one can start with designed values; however the capacitor is usually chosen variable to make fine-tuning easier. Once the right capacitance was found, it can be switched with a fixed capacitor. The first step is to tune and match the proton coil to the right frequency (200.228MHz). Then, the phosphorus coil is placed in the center, and the variable capacitor of the trap is tuned, such that proton coil resonance ($S_{11}$ or $S_{21}$ as measured by a pick-up loop) goes back to where it was before adding the phosphorus coil; i.e. phosphorus coil should be invisible to the proton coil, at the proton frequency. Having two coils present from the beginning and tuning the trap to get the desired resonance frequency will be incorrect; since the obtained tuning might be a result of unresolved coupling. It is notable that this process of proper trap tuning is dependent on the modular design previously mentioned. Figure III-8 shows the proton field across the coil at different configurations, measured at 2.5 cm height above the coil surface, obtained by exciting the proton coil using a cable and moving a pick up loop in 0.5 cm steps. The figure verifies the field degradation that accompanies adding the untrapped phosphorus coil and verifies the fact that adding a trap at the proton frequency on the phosphorus coil effectively blocks the counter-productive currents, allowing for the performance of the proton coil to be maintained. Note that coil tuning/matching needs to be maintained at each scenario.

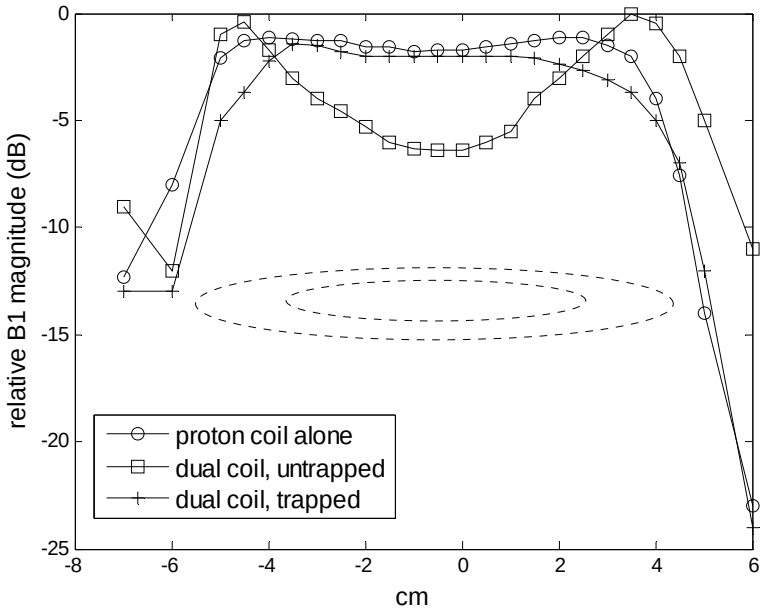


Figure III-8 - Proton field magnitude across the coil. Using the trap effectively restores the proton magnetic field in the center.

*Q measurements*

Since the trap circuit is placed directly in the path of current, any loss in the inductor used will affect the quality factor of the phosphorus coil. Knowing that SNR is proportional to inverse square root of ohmic loss R [26]:

$$SNR = \frac{\sqrt{2}\omega_0 \Delta V M_{xy} |B_{1t}|}{\sqrt{4kT\Delta f R}} \tag{35}$$

Reduction in Q means reduction in SNR and coil sensitivity. Alecci reports the loaded Q of his sodium coil being reduced from 80 to 65 as a result of introducing the

trap (implying a proportional loss in SNR). Capacitors are high-Q components, so the inductor used in the trap is indeed the Q bottleneck.We used an air-core, six turn 22nH inductor (Coilcraft, Cary, IL) which provides a high Q ( datasheet specifications are shown in Figure III-9).

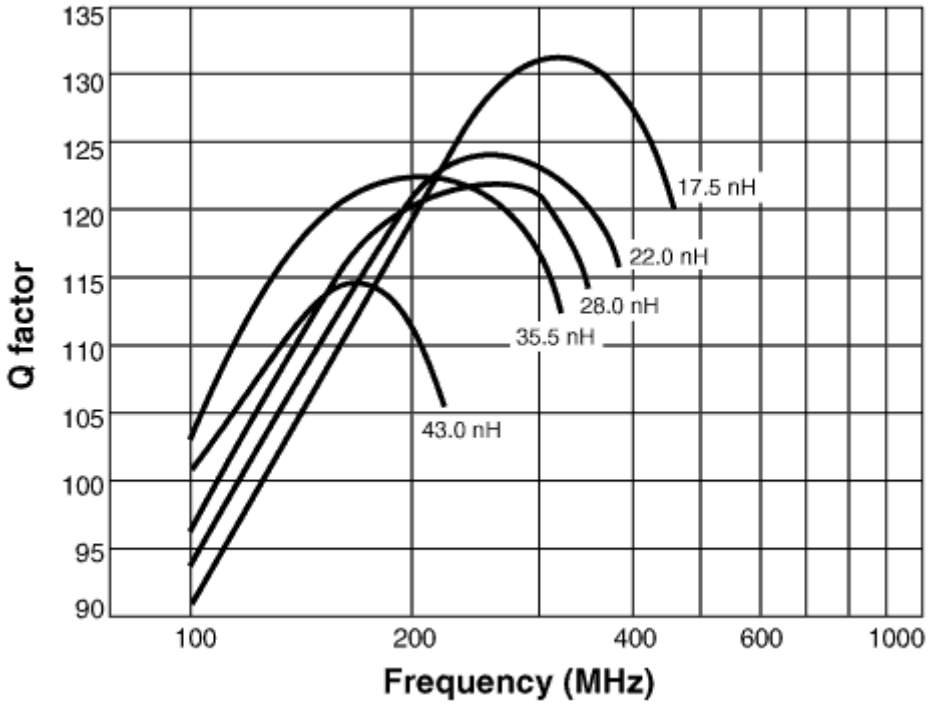


Figure III-9 – Q factor of the inductor (22nH) used to make the trap. Courtesy of Coilcraft, Inc.

To measure the Q of the coil, the cables were removed (since cable loss would be fixed in either case, and to eliminate any radiation losses) and dual pick-up loops were used at about 2cm above the coil. The unloaded to loaded Q was measured as 105/60, and it did not change after introducing the trap. This means the trap loss is negligible compared to the coil/sample loss in this case. We believe that this is due primarily to the

use of high-quality components. No change in loaded Q ensures that there will be no SNR drop due to trap circuit losses.

## III.5. SNR Model

### *III.5.1 $B_1$ Magnitude*

Again considering two coupled loops (Figure III-10), with the first one tuned to $^{1}H$ and the second one tuned to $^{31}P$, the induced current in the phosphorus coil can be calculated as:

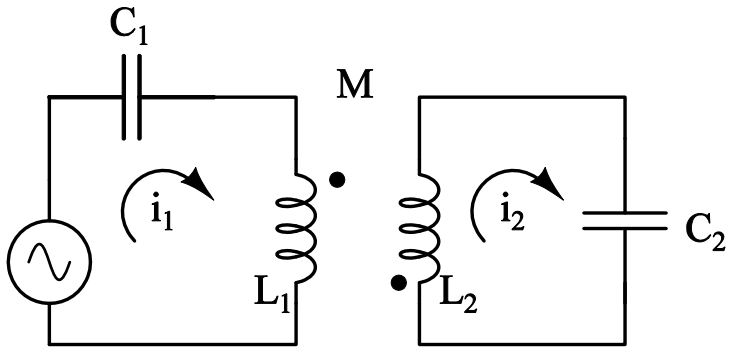


Figure III-10 – Coupled dual-tuned resonators.

$$\frac{i_2}{i_1} = -\frac{X_M}{X_{L_2} + X_{C_2}} = -\frac{X_M}{L_2\omega - \frac{1}{C_2\omega}} \tag{36}$$

$$\frac{i_2}{i_1} = -\frac{M\omega^2}{L_2(\omega^2 - {\omega_2}^2)} \tag{37}$$

with $\omega_2$ being the resonance frequency of the second loop, i.e. phosphorus in our case, in absence of coupling (81.45 MHz at 4.7T). As previously discussed, considering the higher frequency mode (proton), $(\omega^2 - {\omega_2}^2)$ will be negative, indicating an induced current at -180 degrees from the excitation current, which will oppose the proton magnetic field. The total magnetic field at the distance $h$ on the axis will thus be [27]

$$B\left(\frac{Tesla}{Amp.}\right) = \frac{\mu_0}{2}\left(\frac{a^2}{(a^2+h^2)^{3/2}} - \frac{M\omega^2}{L_2(\omega^2 - {\omega_2}^2)} \cdot \frac{b^2}{(b^2+h^2)^{3/2}}\right) \tag{38}$$

according to Biot-Savart, where $a$ = radius of the $^{1}$H (outer) coil and $b$ = radius of the $^{31}$P (inner) coil.

The mutual inductance between two circular loops can be approximated as [28]

$$M = \mu_0\sqrt{ab}\frac{2}{k}\left(\left(1 - \frac{k^2}{2}\right)K(k) - E(k)\right), k = \sqrt{\frac{4ab}{(a+b)^2 + d^2}} \tag{39}$$

where $K(k)$ and $E(k)$ are complete elliptic integrals of the first and second kind (respectively), and $d$ is equal to distance between two planes, which is zero in co-planar design. By measuring the $L_2$=155nH, we can plot the total magnetic field intensity on the axis (Figure III-11).

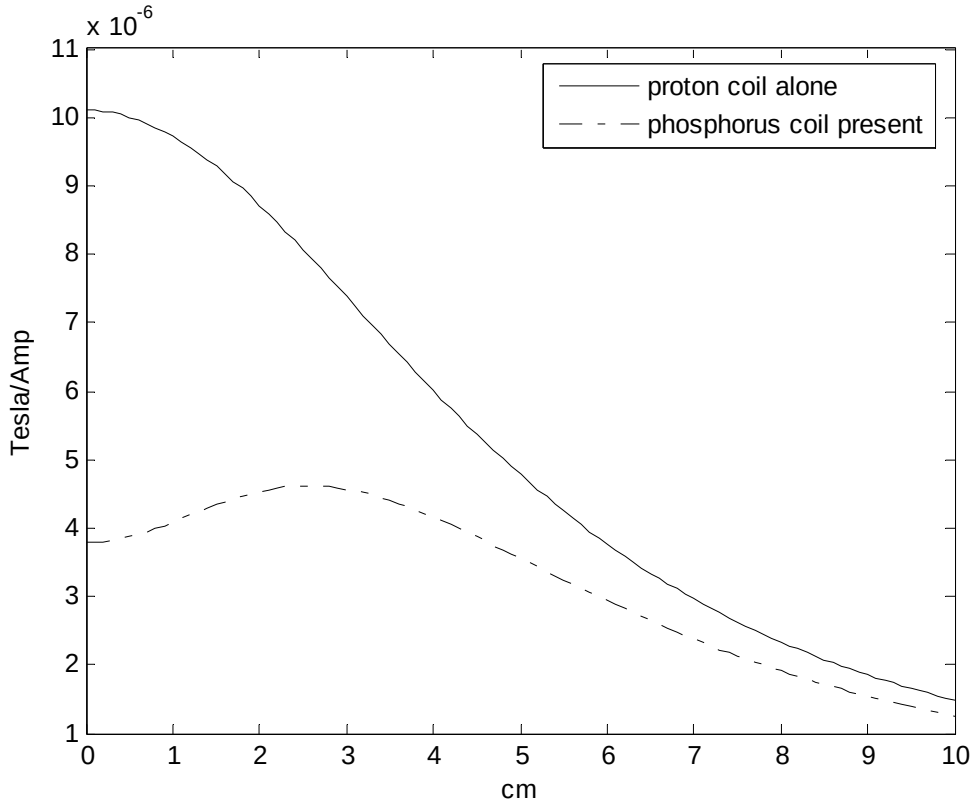


Figure III-11 - Effect of $^{31}$P coupling in $^{1}$H coil field strength along the axis. Coil diameters are 7.1 cm for $^{31}$P and 12.44cm for $^{1}$H.

In order to model the trap effect on the proton $B_1$ magnitude, we can find the effective impedance of a non-ideal trap using equation (28), which is dependent on the frequency, the quality factor (Q), and inductor value (L). Using a low-Q inductor reduces the effective trap impedance. Considering a fixed Q (Figure III-9), the trap impedance will be proportional to the inductor value (however this will introduce loss in the $^{31}$P coil; see Section III.5.2). To model the Q effect on blocking effectiveness of the trap, we can modify the equivalent circuit used earlier to include the trap impedance (Figure III-12).

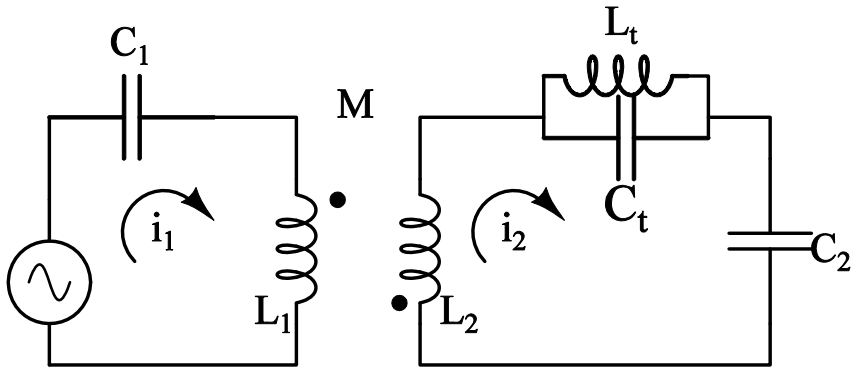


Figure III-12 – Coupled dual-tuned resonators with a trap included.

The current ratio will then be

$$\frac{i_2}{i_1} = \frac{-jX_M}{j(X_{C2} + X_{L2}) + R_t}$$

where $R_t = Q\omega_{trap}L_{trap}$.

Total magnetic field magnitude on the axis will then be

$$B\left(\frac{Tesla}{Amp.}\right) = \frac{\mu_0}{2}\left(\left|\frac{a^2}{(a^2+h^2)^{3/2}} - \frac{jM\omega}{jL_2\frac{(\omega^2-\omega_2{}^2)}{\omega}+R_t}\cdot\frac{b^2}{(b^2+h^2)^{3/2}}\right|\right)$$

For a trap made using a 22nH inductor, field intensity can be found for various Q options along the axis (shown in Figure III-13). It is noted that trap Q does not have a significant effect. This is because once we put resistive impedance in series with the reactance of the coil, the induced current is no longer -180 degrees; but close to -90 degrees. So it will not degrade the field magnitude as badly as it would for low-loss case. However, it could affect the Q of the $^1$H coil.

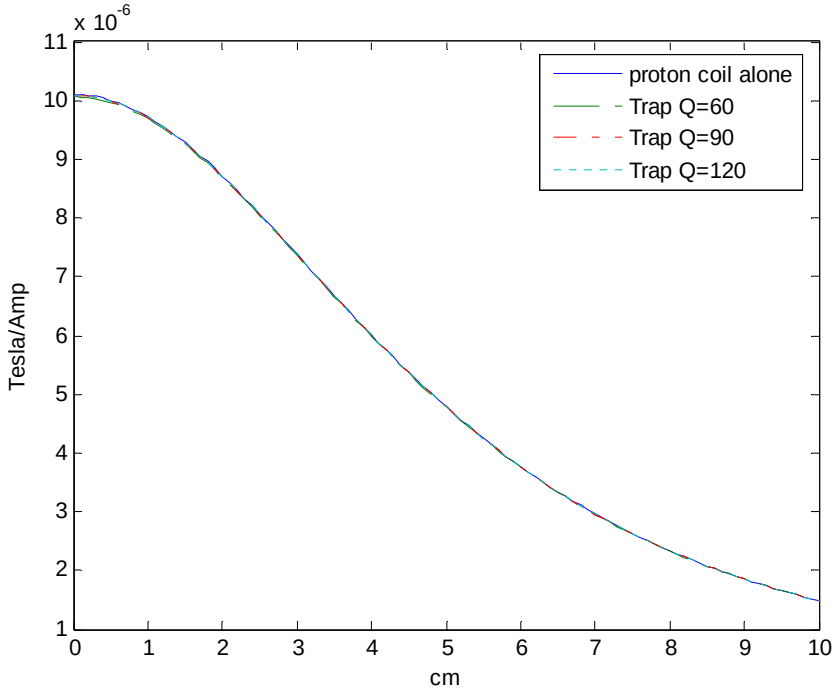


Figure III-13 – Effect of the trap Q on proton field magnitude. Note that all four curves are nearly the same.

*III.5.2 Noise Level*

Inductors are usually considered to be lossy elements. Adding lossy elements to the coil resonator introduces thermal noise, which degrades coil sensitivity or SNR. Considering the $B_1$ per unit current to be equal in both cases, sensitivity ratio, defined as SNR of the untrapped coil divided by SNR of the trapped coil, will be

$$\frac{SNR_{trapped}}{SNR_{untrapped}} = \sqrt{\frac{r_c}{r_t + r_c}} = \sqrt{\frac{1}{\frac{r_t}{r_c} + 1}} \tag{40}$$

where $r_c$ is the resistance of the coil conductor and $r_t$ is the effective trap resistance being added to the system.

At the $^{31}$P frequency, using equation (26), the effective trap resistance $r_t$ appearing in series with the coil resistance will be equal to the actual trap inductor resistance (with a very good approximation; since the trap is far away from resonance). Equation (40) becomes

$$\frac{SNR_{trapped}}{SNR_{untrapped}} = \sqrt{\frac{1}{\frac{L_t}{L_c} \cdot \frac{Q_c}{Q_t} + 1}} \tag{41}$$

where $L_t$ is the inductor value used in the trap, $Q_t$ is the Q of the trap, $L_c$ is the $^{31}$P coil inductance, and $Q_c$ is the loaded $^{31}$P coil Q, before introduction of the trap.

At the $^{1}$H frequency, using equation (29) to transform the resonant trap resistance $R = Q_t\omega_0 L_t$ to the proton side of the circuit, effective trap resistance can be found as:

$$r_t = \frac{{X_M}^2 R}{R^2 + {X_2}^2} \tag{42}$$

where $X_M$ is the mutual reactance at $^{1}$H frequency, and $X_2$ is the reactance of the $^{31}$P coil at $^{1}$H frequency. Assuming $X_2 \ll R$:

$$r_t = \frac{{X_M}^2}{Q_t\omega_0 L_t} \tag{43}$$

equation (40) becomes

$$\frac{SNR_{trapped}}{SNR_{untrapped}} = \sqrt{\frac{1}{\frac{M^2}{L_c \cdot L_t} \cdot \frac{Q_c}{Q_t} + 1}} \tag{44}$$

where $M$ is the mutual inductance between the two coils, $L_t$ is the inductor value used in the trap, $Q_t$ is the Q of the trap, $L_c$ is the $^{1}$H coil inductance, and $Q_c$ is the loaded $^{1}$H coil Q, before introduction of the trap. It is noteworthy that performance of the $^{31}$P is coil is inversely proportional to the trap inductance, while performance of the $^{1}$H coil is proportional to the trap inductance (see Figure III-14). Therefore, a design compromise has to be made on choice of the inductor, depending on whether performance at the $^{31}$P or $^{1}$H frequency needs to be optimized. In this work, L = 22nH was used, in order to keep both sensitivities above 95%. Also, larger Q provides better performance for both nuclei (Figure III-15).

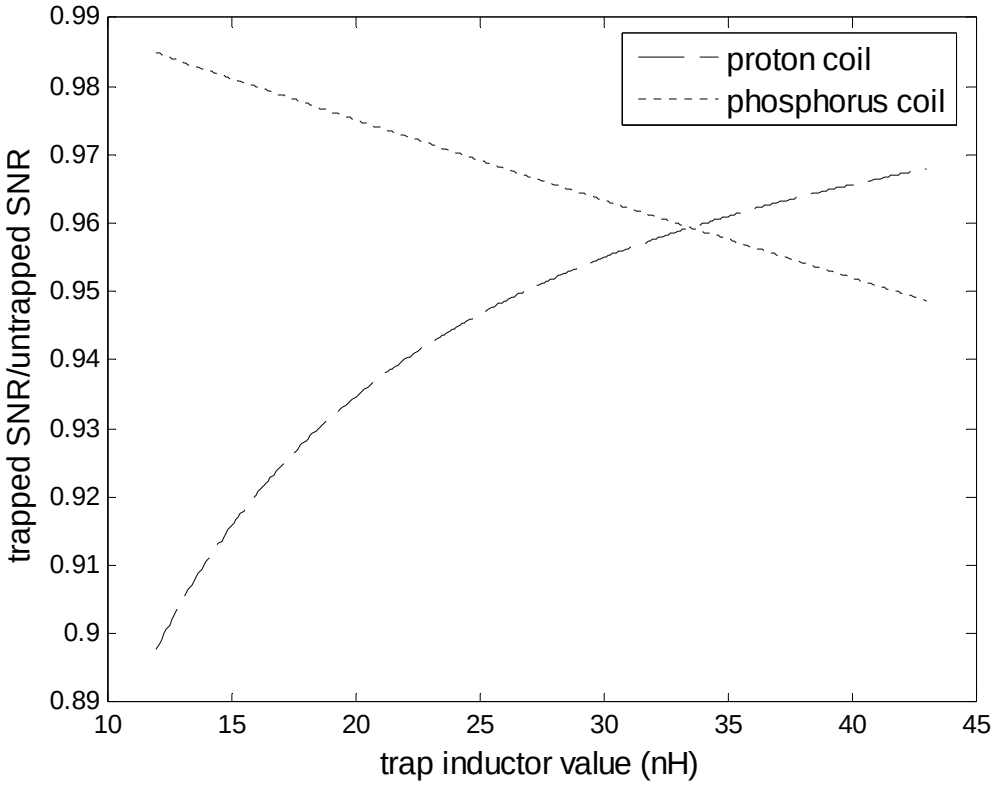


Figure III-14 – Effect of the trap inductor value on coil performance. A quality factor Q=150 is assumed.

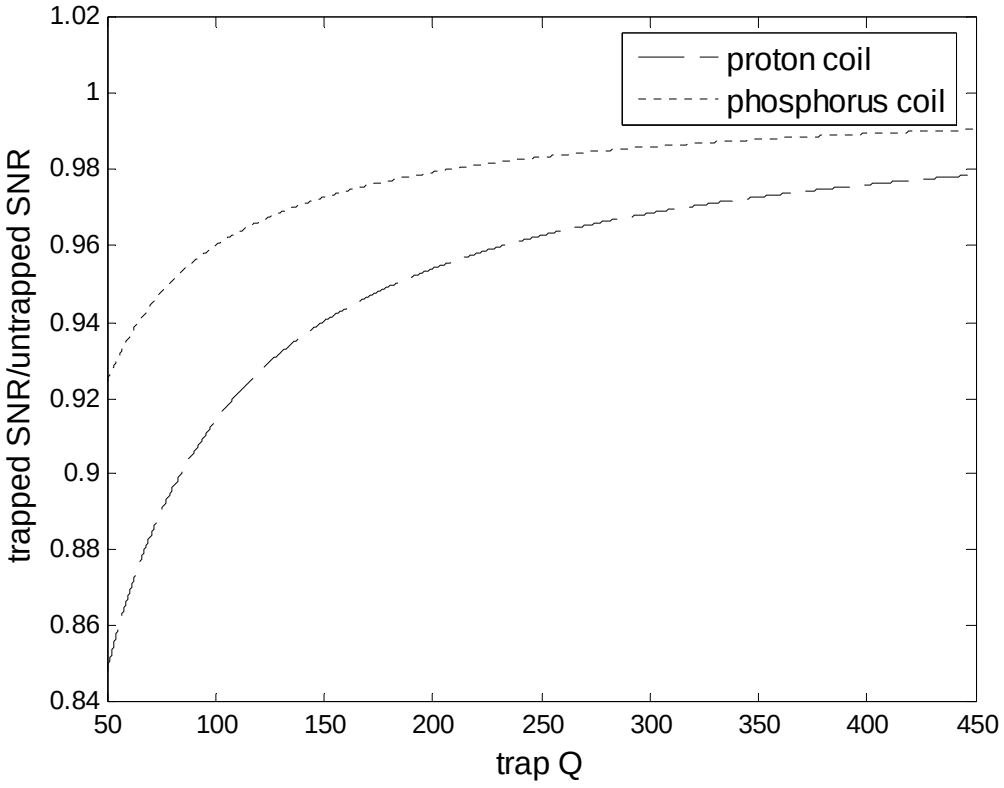


Figure III-15 - Effect of the trap Q value on coil performance. A fixed trap inductor value of L=22nH is assumed.

# CHAPTER IV

# MRI/MRS TESTING

In this chapter, we examine use of MR images and spectra as indices for coil performance, and discuss the methodology of performing spectroscopy on the laboratory Varian Inova system

## IV.1. Spectroscopy Using the Varian Inova System

A 4.7 Tesla, 33 cm Varian Inova MR system located in the Magnetic Resonance Lab at Texas A&M University was used for all data acquisition.

### *IV.1.1 System Modifications*

Pulsed spectroscopy is performed in a similar fashion to imaging; however certain system modifications need to be done. There are certain hardware components (besides the RF coil, obviously) that are frequency-selective; for example, to operate the same coil in both transmit and receive mode, a T/R switch is used, containing a quarter-wavelength transmission line segment, keeping the transmit power from getting into receive circuitry. For each nucleus being interrogated, the quarter-wavelength needs to be adjusted based on the Larmor frequency of that nucleus. For example, the 25 cm RG-58 cable normally used for $^{1}$H (200MHz at 4.7T) needs to be switched with a 62 cm one for $^{31}$P(81.05MHz at 4.7 T). The 200MHz balun in line to the transceiver needs to be bypassed. Also, a bandpass filter is used at the input to the RF amplifier to minimize

unwanted tones. Normally a Mini-Circuits (Brooklyn, NY) low-pass 0-200 MHz filter is used for proton; it was switched with a SIF-70 bandpass filter for phosphorus.

### *IV.1.2 Shimming*

Inhomogeneity in $B_0$ results in added frequency components in the received free-induction-decay (FID) signal. When imaging, those shifts are usually powered by the gradients, however in spectroscopy, small shifts will show up next to the main peak, broadening its line, reducing the peak value (since the signal is divided over a range of frequencies) and hiding spectral information. Therefore proper shimming of the static B field is essential prior to spectroscopy.

For in-vivo experiments on brain and liver tissues, shimming to less than 0.1 ppm is required[29]; however for phantom studies where chemical shifts are several ppms apart, about 1 ppm resolution is sufficient. Since the signal intensity acquired from phosphorus atoms is much weaker than hydrogen, one can do the shimming on water first (using the $^{1}H$ coil), and then switch the coils without moving the phantom. This is indeed one of the benefits of having a dual-tuned coil with two inputs. In our experiments, shimming was accomplished to less than 50 Hz FWHM (see Figure IV-1).

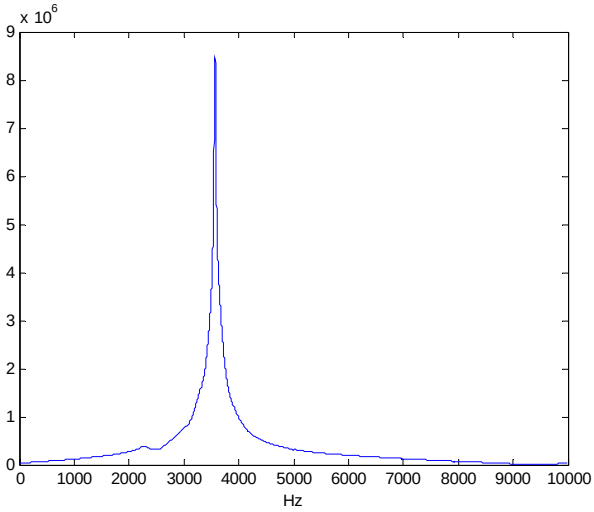


Figure IV-1 – $^{1}H$ spectra obtained to measure linewidth after shimming. For acquiring phosphorus spectra, the linewidth was shimmed to less than 50Hz (0.62ppm).

A phantom composed of three isolated chambers containing three phosphorus compounds with different chemical shifts, mimicking those of common biological phosphorus content [30], was used to acquire test spectra (Figure IV-2). Each chamber is 58 mm wide and 8 mm deep. From bottom to top, the chambers contain 1 M phenyl phosphonic acid ($C_6H_7O_3P$), 0.5M potassium phosphate ($K_2HPO_4$), 0.5M disodium pyrophosphate ($Na_2H_2P_2O_7$). A test tube containing 1.5M phosphoacetic acid ($C_2H_5O_5P$) was also placed underneath the coil. (It is sometimes used for in vivo studies as a chemical shift reference, in a small capillary). Figure IV-3 shows sample spectra obtained for 10 kHz spectral width. Other parameters will be described in detail later.

Figure IV-2 – The three-chamber phantom used for spectroscopy. Contains three phosphorus compounds with different chemical shifts that mimic biological content.

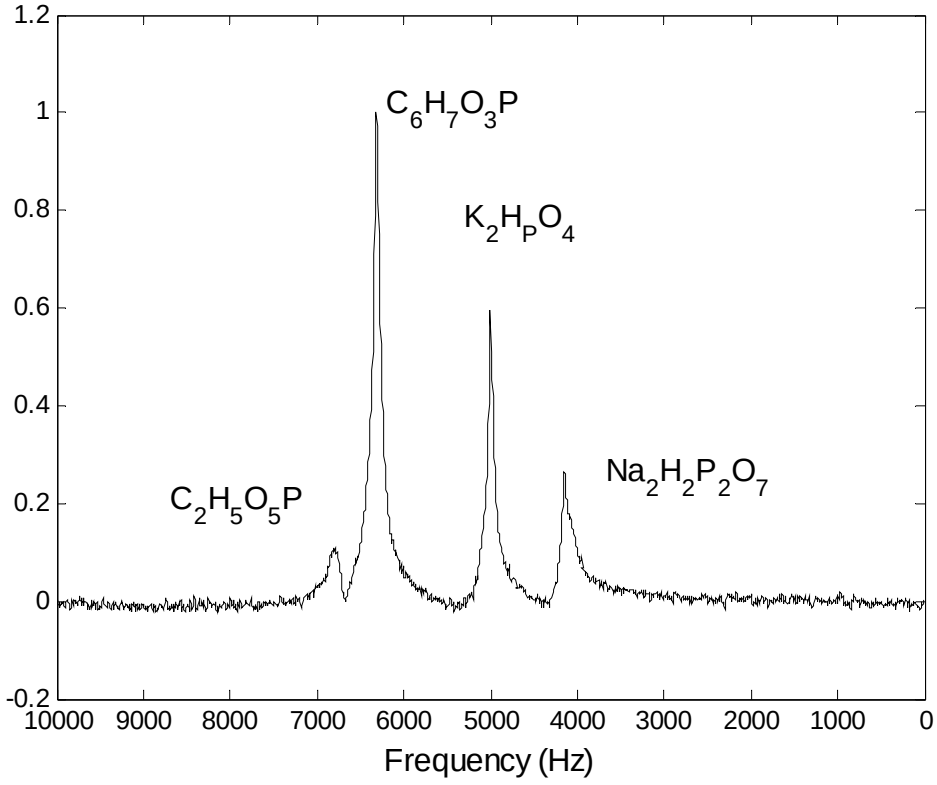


Figure IV-3 – Sample spectra obtained from the physiological phosphorus phantom. Acquisition parameters are described in detail later.

*Effects of pulse width/power*

Among the parameters that need to be set are the duration of the pulsewidth and transmitted power required to obtain a 90 tip angle. During application of a RF pulse, the rotational frequency of the net magnetization vector is given by

$$\Omega = \gamma B_1 \tag{45}$$

where $B_1$ is the effective field for the polarization being used. The tipped angle following $\tau$ seconds of radiation is given by

$$\alpha = \int_0^{\tau} \gamma B_1 \, dt = \gamma B_1 \tau \tag{46}$$

which is proportional to pulse power and duration. In our experiment (using a typical spin echo sequence), since the surface coil field has different field sensitivity at different heights, some chambers might be under-tipped or over-tipped. Adiabatic plane-rotation pulse sequences such as BIR-4 [31] can be used to get homogeneous field at different heights, providing 90 degree tip for the entire sensitive volume of the surface coil. However, using regular rectangular pulses, different peaks on the spectra obtained from an inhomogeneous phantom will be affected by $B_1$ magnitude at that chamber. In Figure IV-4 (a), the first chamber has the tallest peak (closest tip angle to 90), however by doubling the pulsewidth, the second chamber yields the maximum signal, while the first

one over-tips, reducing signal strength during readout. In our acquisitions, pulsewidth was optimized for the first chamber.

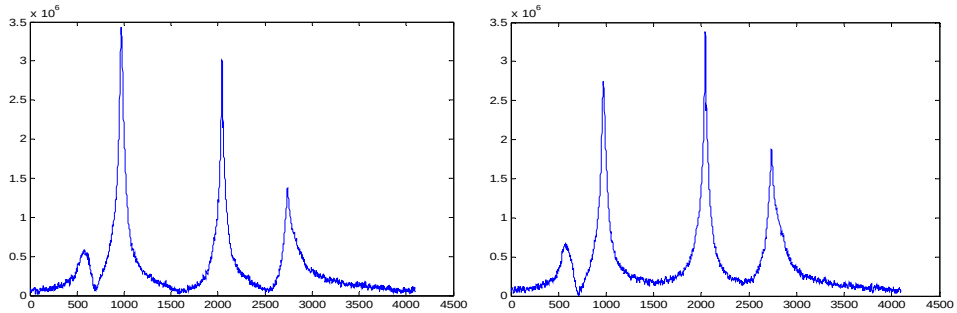


Figure IV-4 – Effect of power on spectra obtained from an inhomogeneous phantom. (a): pulsewidth optimized for the first chamber. (b): pulsewidth optimized for the second chamber.

One can calibrate the pulsewidth to get maximum signal. To do so, first we needed to narrow the spectral width down to a single peak (first chamber; second peak from the left). Then, set an array of pulsewidths ranging from 20 to 400 μs, and then manually compared the array of signals. Figure IV-5 shows the maximum signal occurring at about 200 μs.

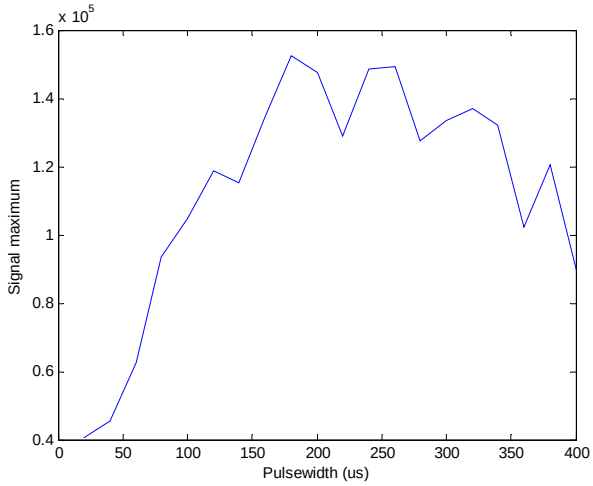


Figure IV-5 – Maximum signal over pulsewidths ranging from 20 to 400 μs used for 90 degree pulsewidth calibration.

### *IV.1.3 Effect of Averaging (transients)*

If we repeat the acquisition $n$ times and sum the resulting FID signals, the signal voltage magnitude will increase $n$ times, while the noise voltage will increase only $\sqrt{n}$ times (being stochastic process, it is the noise powers that add up, instead of voltages). So the overall SNR will increase $\frac{n}{\sqrt{n}} = \sqrt{n}$ times. This technique can be used to decrease the noise effect, especially in weak nuclei, at the expense of increased acquisition time. In Figure IV-6, two spectra are acquired; the right one averaged four times more than the left.. The left spectrum has SNR = 8.7, while the right one has SNR=16.8, almost twice.

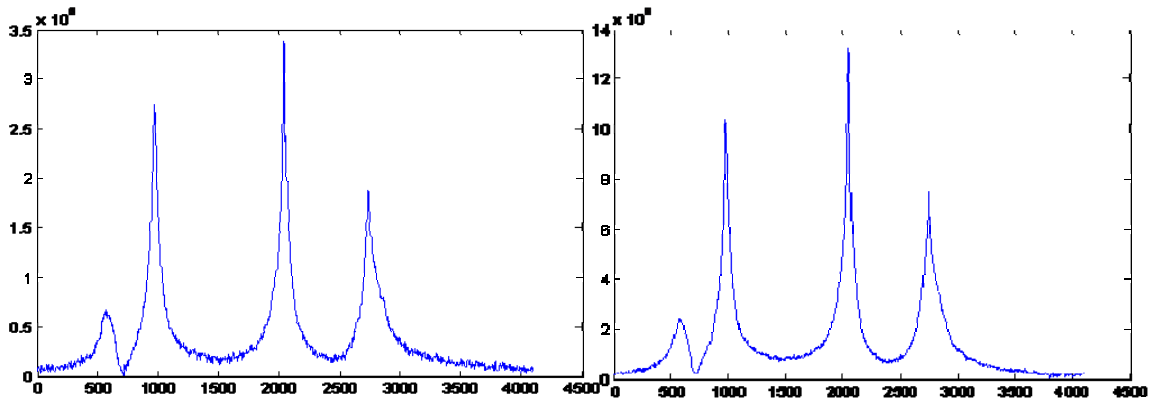


Figure IV-6 – Effect of averaging on spectra. Left: spectrum acquired with 128 averages; SNR=8.7
Right: 512 averages; SNR=16.8 .

### *IV.1.4 Exponential Line-broadening (apodization) Filters*

Since the number of data points is limited, there will be artifacts caused by early truncation of the FID. If we multiply the time-domain signal (FID) by a decaying exponential function before taking the Fourier transform, strong signals remain unaffected while noise levels are attenuated, at the expense of increase in linewidth. Two common time-domain filter functions are exponential and Lorentz-Gauss filters.

An exponential time-domain filter function is given by

$$f(t) = e^{-\frac{t}{T_w}} \tag{47}$$

A Lorentz-Gauss filter [32] is given by

$$f(t) = e^{\frac{t}{T_w}} e^{-\frac{t^2}{T_g{}^2}} \tag{48}$$

In exponential filtering, $\lambda = \frac{1}{T_w}$ is the line-broadening factor, adding to the spectrum linewidth. Maximum SNR for a peak is obtained by "matched filtering" where $\lambda$ is chosen equal to the FWHM; at the expense of doubling the linewidth. In our case, since FWHM=50 Hz, choosing $\lambda$ =10 Hz provides acceptable SNR without significant loss of resolution. Figure IV-7 shows the effect of 10 Hz exponential apodization.

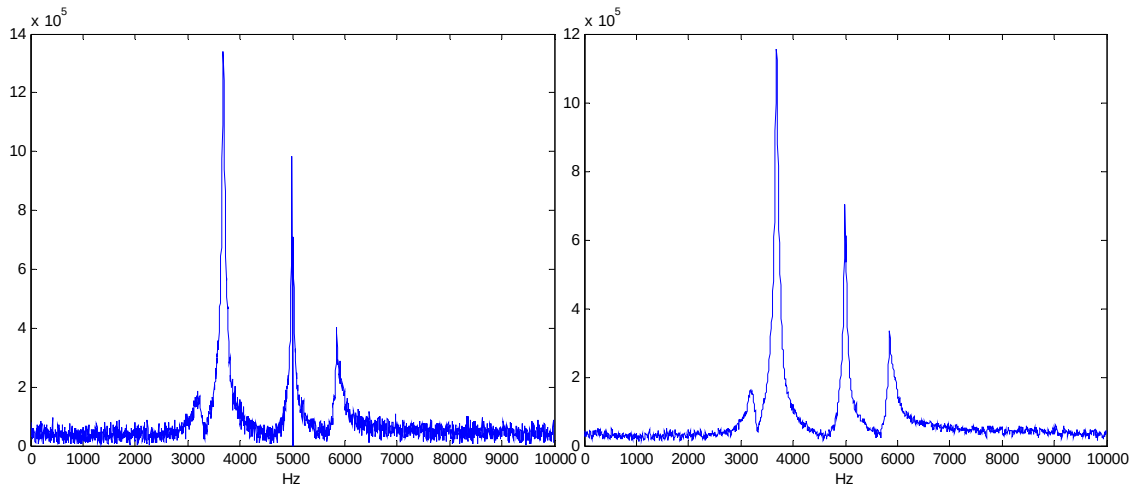


Figure IV-7 – Effect of time-domain filtering on spectra. Left: spectrum with no apodization. Right: spectrum with 10 Hz exponential apodization.

## IV.2. Trap Analysis

### *IV.2.1 Comparison Methodology*

The effect of putting on the trap needs to be assessed on the $^{31}$P coil itself (by comparing spectra acquired at different trap scenarios), and on the $^{1}$H coil around it (by

comparing proton field map images acquired at different trap scenarios). The following set of data were thus acquired:

1. Proton coil with no phosphorus coil present (as the control experiment). Shimming is performed; transmitted 90/180 pulse power is optimized (to provide enough penetration without over-tipping), and kept constant for the next scenarios.

2. The next step was to add the phosphorus coil with no trap in place, and acquire a proton image and phosphorus spectra. Note that in this case, since the two coils are coupled, they will not tune independently. However since the effect of coupling on resonance frequency shift is much higher at the $^{1}H$ mode than $^{31}P$, the $^{31}P$ coil was re-tuned first, and then $^{1}H$ coil.

There was a jumper placed across the trap, to enable shorting it out without moving the setup. A plug-in 68pF capacitor across one of the gaps also needed to be removed, to enable restoring the tune on the $^{31}P$ coil with the trap in place. It is important that change of trap is done without moving the setup, in order to preserve the shim and make the results comparable.

3. After removing the jumper and enabling the trap, images and spectra were acquired with the same parameters as step 1 and 2 (41/47 dB transmitter power). Note that it is essential to keep the power fixed for all 3 scenarios; since re-optimizing power could mask the SNR loss we are investigating.

The results from these experiments are divided into (proton) image results and phosphorus spectra results. The findings are detailed below, but in summary conclude that:

1. The trap can be added to the phosphorus coil without significantly affecting its performance

2. An untrapped phosphorus coil used in conjunction with a proton coil significantly affects the field pattern of the proton coil and

3. A trapped coil used in conjunction with a proton coil maintains the expected proton coil performance.

### *IV.2.2 Results: Spectra*

Figure IV-8 shows the two spectra obtained without and with the trap in place. The spectra were obtained from the same 3-chamber phantom, but without the reference compound previously included (the first peak on the left in the previous figures). In addition, an SNR issue with the system T/R switch was corrected, providing superior SNR to the previous spectra. The parameters input into the 'spuls' imaging sequence on the Varian were as follows: sw = 10kHz, na= 16, tr=20, tpwr=34. To compare SNR, first the dc component was removed, and then peak value was divided by noise RMS value, to provide a measure for SNR (only valid if the two spectra are equally shimmed; in this case, one spectra has FWHM=47Hz, while the other one has FWHM=52 Hz, almost equal). Untrapped spectra had SNR=325, while trapped spectra had SNR=307; about 5% lower, indicating that the trap has a minimal impact on the phosphorus coil performance.

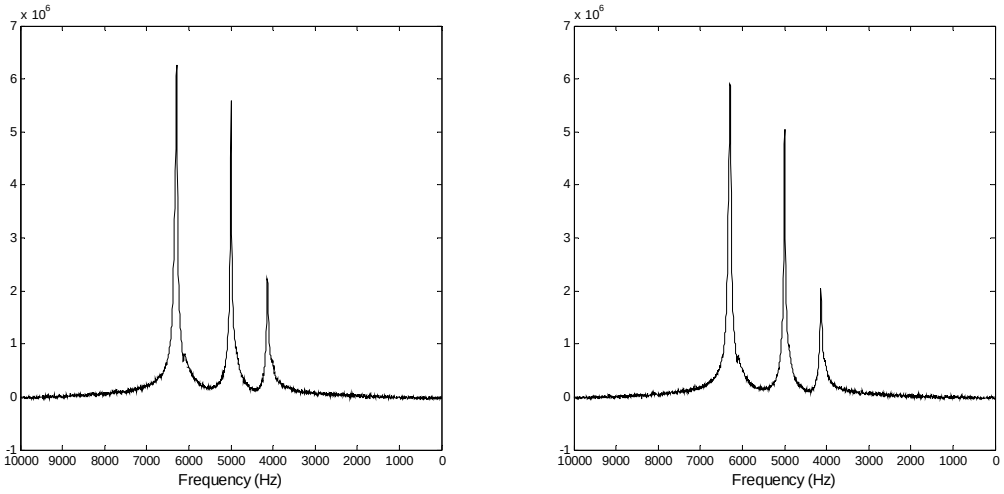


Figure IV-8- $^{31}$P spectra obtained with Left: no trap in place Right: with trap in place. About 5% loss in SNR is observed. (SNR is the ratio of peak value to rms noise )

### *IV.2.3 Results: Proton Imaging*

Figure IV-9 shows the proton images obtained from the surface coil shown in Figure III-3 in the three scenarios described above. The proton coil alone (a) had SNR = 57.7, the proton coil with the untrapped phosphorus coil present had SNR = 20.6, and the proton coil with the phosphorus coil trapped had SNR=53.2 (SNR calculated over the whole phantom, using a histogram method, in which the voxels containing signal over a given threshold are considered as "signal" and the noise region is user-selected).

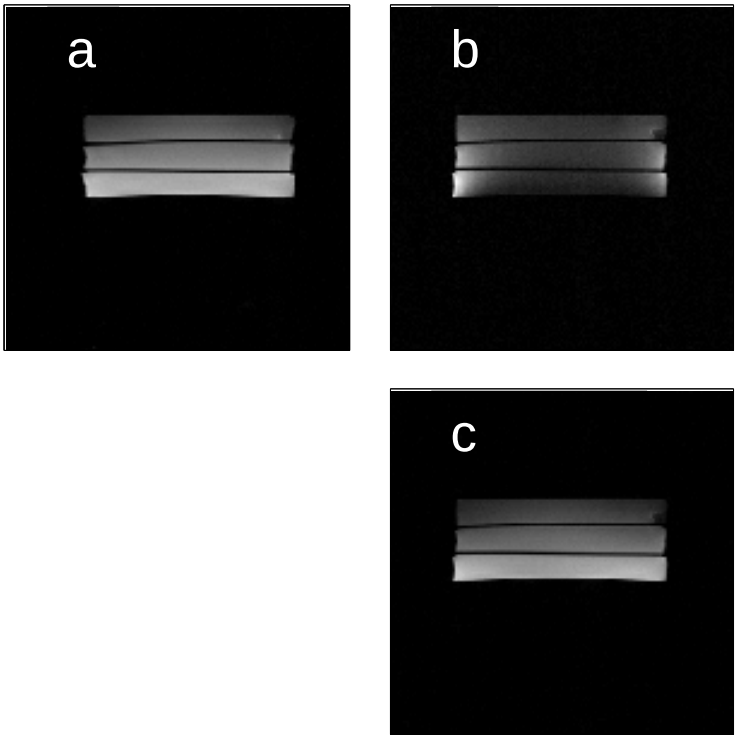


Figure IV-9 – Images obtained from (a): proton coil with no 31P coil present. (b): proton coil with untrapped 31P coil present. (c) proton coil after adding the trap on the 31P coil. The reduced sensitivity area in the center is no longer evident after introducing the trap.

## IV.3. Insertability

We need to show that the trapped $^{31}$P coil can be used with other general-purpose $^{1}$H coils. To do so, a volume $^{1}$H coil (16-rung, highpass birdcage [33] commonly used in the lab) was chosen, and the $^{31}$P coil was placed inside it, making sure that the two fields were not orthogonal (If the fields were orthogonal, then theoretically a trap might not be necessary). The coil setup is shown in Figure IV-10 .

Figure IV-10 – The surface phosphorus coil being used with a proton volume coil.

Proton images were acquired from the volume coil, in the same three scenarios as were used with the surface coil. Figure IV-11 shows the proton images obtained at the three scenarios described. The proton coil alone (a) had SNR = 58.02, the proton coil with untrapped phosphorus coil present had SNR = 41.4, and proton with phosphorus trapped had SNR=54.63 (SNR was calculated over the whole phantom, using the histogram method described before).

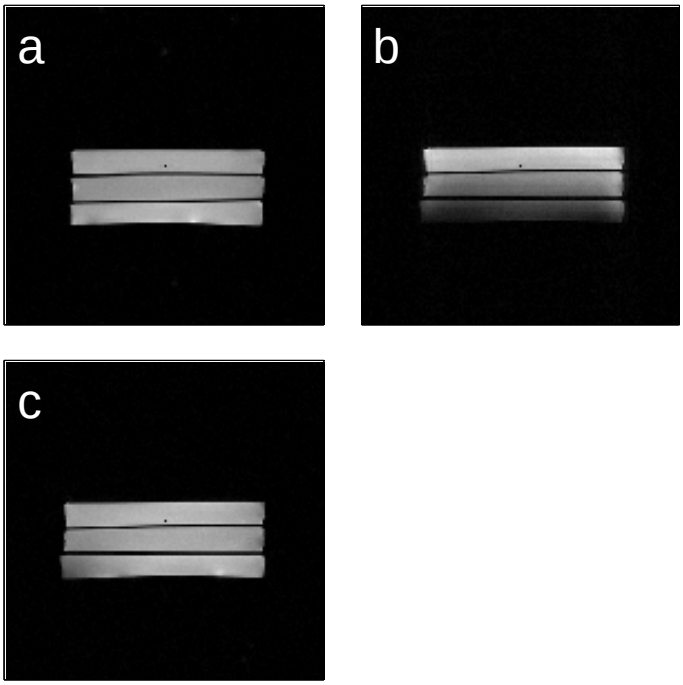


Figure IV-11 - Images obtained from a proton volume coil. (a) no $^{31}$P coil present (b) untrapped $^{31}$P coil present, showing reduced sensitivity (c) trapped $^{31}$P coil present.

Table 3 summarizes the effect of the trap on the SNR of each coil.

Table 3 – Relative SNR obtained at different configurations

| Configuration | Normalized SNR |
|---|---|
| Surface Proton Coil | |
| Single coil | 1.0 |
| Dual coil, no trap | 0.36 |
| Dual coil, trapped | 0.93 |
| Volume Proton Coil | |
| Single coil | 1.0 |
| Dual coil, no trap | 0.71 |
| Dual coil, trapped | 0.95 |
| Phosphorus Coil | |
| No trap | 1.0 |
| With trap | 0.95 |

A three-element phased array coil comprised of loops decoupled by overlap was also built and tested with the $^{31}$P coil on the bench. The array coil is shown in Figure IV-12.

Figure IV-12 – Three-element phased-array proton coil structure.

The untrapped $^{31}$P coil increased the array coupling from an average value of -15 dB to an average value of -9 dB. Elements that were initially decoupled by overlapping, coupled through the $^{31}$P coil. By placing the trap on the phosphorus coil, this problem was resolved as well. The 3x3 coupling matrices for the three different scenarios are shown in Table 4.

Table 4 – Effect of the $^{31}$P coil on element coupling for the proton array coil

| | No $^{31}$P present | Untrapped $^{31}$P present | Trapped $^{31}$P present |
|---|---|---|---|
| Coupling in dB | $\begin{bmatrix} -33 & -18.5 & -17 \\ -18.5 & -36 & -18.5 \\ -17 & -18.5 & -32 \end{bmatrix}$ | $\begin{bmatrix} -27 & -9 & -11.5 \\ -9 & -29 & -10.5 \\ -11.5 & -10.5 & -29 \end{bmatrix}$ | $\begin{bmatrix} -30 & -16 & -17 \\ -16 & -23 & -17 \\ -17 & -17 & -28 \end{bmatrix}$ |

# CHAPTER V

# CONCLUSIONS AND FUTURE WORK

Multi-nuclear MRI and MRS are becoming more prevalent, particularly as MRI field strengths increase, and with it, the promise of clinical spectroscopy. This will demand high-performance, versatile multi-frequency probes. In addition, as field strengths of whole-body magnets increase, proton coil designs are becoming increasingly specialized, usually entailing the use of complex multi-channel array coils that cannot easily be re-engineered for multi-frequency use. In this work, a particular design for a second-nuclei coil using LC traps was implemented and thoroughly examined. A model was developed to analyze the effect of the trap on resonance frequency and SNR of both channels. Experimental MR data was obtained to investigate the performance of this method compared to untrapped cases. The results, which showed a significant degraded sensitivity of the proton coil when an untrapped phosphorus coil was present, explain why untrapped, concentric designs for proton decoupling usually fail to achieve FDA limits for SAR, as the power input to the proton coil is increased in order to compensate for the decreased sensitivity. Also, applicability of the trap method was examined to enable using second-nuclei coils in conjunction with existing proton coils, saving the cost of designing specialized proton coils. Guidelines are provided for trap design, in order to further enhance the performance and insertability.

In general, when migrating from a single-tuned to dual-tuned coil system, performance loss for at least one of the nuclei is unavoidable (regardless of the dual-

tuning scheme used). Methods used in the past usually provide guidelines to optimize the design in favor of the observation channel (less-abundant nuclei), imposing a significant loss (on the order of 50%) on the proton channel. We showed that by using the trap design, performance at both nuclear frequencies can be maintained above 90% of their single-tuned counterparts. Our lab is known for its work in parallel imaging – both multichannel receive and transmit hardware and methodology. The insertability of a second-nuclei coil enabled by the use of a trap should allow for more straightforward incorporation of spectroscopy studies into our lab's existing array coil studies, opening the way for a variety of future work, such as in vivo $^{31}P$ magnetic resonance spectroscopy. Also, this method is applicable in higher frequency RF coil designs, of particular interest with the increasing availability of higher field magnets.

## REFERENCES

[1] T. Toyooka, K. Nagayama, J. Suzuki, and T. Sugimoto, Noninvasive assessment of cardiomyopathy development with simultaneous measurement of topical H-1 and P-31 magnetic resonance spectroscopy. Circulation 86 (1992) 295-301.

[2] P.A. Bottomley, and R.G. Weiss, Non-invasive magnetic-resonance detection of creatine depletion in non-viable infarcted myocardium. Lancet 351 (1998) 714-718.

[3] J.W. Hugg, G.B. Matson, D.B. Twieg, A.A. Maudsley, D. Sappeymarinier, and M.W. Weiner, P-31 MR spectroscopic imaging (MRSI) of normal and pathological human brains. Magnetic Resonance Imaging 10 (1992) 227-243.

[4] W. Negendank, Studies of human tumors by MRS - a review. NMR in Biomedicine 5 (1992) 303-324.

[5] D.J. Griffiths, Introduction to electrodynamics, Prentice Hall, Upper Saddle River, NJ, 1999.

[6] A.J. Shaka, J. Keeler, T. Frenkiel, and R. Freeman, An improved sequence for broad-band decoupling - Waltz-16. Journal of Magnetic Resonance 52 (1983) 335-338.

[7] H. Bomsdorf, P. Roschmann, and J. Wieland, Sensitivity enhancement in whole-body natural abundance C-13 spectroscopy ssing C-13/H-1 double-resonance techniques at 4-Tesla. Magnetic Resonance in Medicine 22 (1991) 10-22.

[8] M.D. Schnall, V.H. Subramanian, J.S. Leigh, and B. Chance, A new double-tuned probe for concurrent H-1 and P-31 NMR. Journal of Magnetic Resonance 65 (1985) 122-129.

[9] M. Schnall, NMR, basic principles and progress. Edited by Diehl, P, Springer-Verlag, Berlin, 1992.

[10] M. Decorps, P. Blondet, H. Reutenauer, J.P. Albrand, and C. Remy, An Inductively coupled, series-tuned NMR probe. Journal of Magnetic Resonance 65 (1985) 100-109.

[11] D.I. Hoult, and B. Tomanek, Use of mutually inductive coupling in probe design. Concepts in Magnetic Resonance 15 (2002) 262-285.

[12] D.I. Hoult, The NMR receiver: A description and analysis of design. Progress in Nuclear Magnetic Resonance Spectroscopy 12 (1978) 41-77.

[13] G.B. Matson, P. Vermathen, and T.C. Hill, A practical double-tuned H-1/P-31 quadrature birdcage headcoil optimized for P-31 operation. Magnetic Resonance in Medicine 42 (1999) 173-182.

[14] J. Murphyboesch, R. Srinivasan, L. Carvajal, and T.R. Brown, Two configurations of the four-ring birdcage coil for $^{1}$H imaging and $^{1}$H-decoupled $^{31}$P spectroscopy of the human head. Journal of Magnetic Resonance, Series B 103 (1994) 103-114.

[15] V.R. Cross, R.K. Hester, and J.S. Waugh, Single coil probe with transmission-line tuning for nuclear magnetic double-resonance. Review of Scientific Instruments 47 (1976) 1486-1488.

[16] M.E. Stoll, A.J. Vega, and R.W. Vaughan, Simple single-coil double-resonance NMR probe for solid-state studies. Review of Scientific Instruments 48 (1977) 800-803.

[17] G. Annaert, A. Barel, R. Luypaert, M. Osteaux, and J. Renneboog, A low-lossy double tuned resonator for concurrent $^{1}$H and $^{31}$P nuclear magnetic resonance, Instrumentation and Measurement Technology Conference, 1989. IMTC-89. Conference Record., 6th IEEE, 1989, pp. 190-193.

[18] F.D. Doty, R.R. Inners, and P.D. Ellis, A multi-nuclear double-tuned probe for applications with solids or liquids utilizing lumped tuning elements. Journal of Magnetic Resonance 43 (1981) 399-416.

[19] J.R. Fitzsimmons, H.R. Brooker, and B. Beck, A transformer-coupled double-resonant probe for NMR imaging and spectroscopy. Magnetic Resonance in Medicine 5 (1987) 471-477.

[20] J.R. Fitzsimmons, B.L. Beck, and H.R. Brooker, Double resonant quadrature birdcage. Magnetic Resonance in Medicine 30 (1993) 107-114.

[21] P.A. Bottomley, C.J. Hardy, P.B. Roemer, and O.M. Mueller, Proton-decoupled, Overhauser-enhanced, spatially-localized C-13 spectroscopy in humans. Magnetic Resonance in Medicine 12 (1989) 348-363.

[22] H. Merkle, H.R. Wei, M. Garwood, and K. Ugurbil, $B_1$-insensitive heteronuclear adiabatic polarization transfer for signal enhancement. Journal of Magnetic Resonance 99 (1992) 480-494.

[23] G. Adriany, and R. Gruetter, A half-volume coil for efficient proton decoupling in humans at 4 Tesla. Journal of Magnetic Resonance 125 (1997) 178-184.

[24] W. Durr, and S. Rauch, A dual-frequency circularly polarizing whole-body MR antenna for 69/170 MHz. Magnetic Resonance in Medicine 19 (1991) 446-455.

[25] M. Alecci, S. Romanzetti, J. Kaffanke, A. Celik, H.P. Wegener, and N.J. Shah, Practical design of a 4 Tesla double-tuned RF surface coil for interleaved H-1 and Na-23 MRI of rat brain. Journal of Magnetic Resonance 181 (2006) 203-211.

[26] S.M. Wright, and L.L. Wald, Theory and application of array coils in MR spectroscopy. Nmr in Biomedicine 10 (1997) 394-410.

[27] J. Mispelter, B. Tiffon, E. Quiniou, and J.M. Lhoste, Optimization of C-13-(H-1) double coplanar surface-coil design for the waltz-16 decoupling sequence. Journal of Magnetic Resonance 82 (1989) 622-628.

[28] F.W. Grover, Inductance calculations, working formulas and tables, D. Van Nostrand company, inc., New York, 1946.

[29] G.B. Peter R. Luyten, Frenk M. Sloff, Jan W. A. H. Vermeulen, Jan I. Van Der Heijden, Jan A. Den Hollander, Arend Heerschap, Broadband proton decoupling in human $^{31}$P NMR spectroscopy. NMR in Biomedicine 1 (1989) 177-183.

[30] K. Hendrich, H.Y. Liu, H. Merkle, J. Zhang, and K. Ugurbil, $B_1$ voxel shifting of phase-modulated spectroscopic localization techniques. Journal of Magnetic Resonance 97 (1992) 486-497.

[31] M. Garwood, and K. Yong, Symmetrical pulses to induce arbitrary flip angles with compensation for RF inhomogeneity and resonance offsets. Journal of Magnetic Resonance 94 (1991) 511-525.

[32] R.A. De Graaf, In vivo NMR spectroscopy : principles and techniques, Wiley, Chichester ; New York, 1998.

[33] M.P. McDougall, D.G. Brown, D.K. Spence, and S.M. Wright, A low-pass trombone birdcage coil with broad tuning range, Proc. Intl. Soc. Mag. Reson. Med, 2001, pp. 1092.

# VITA

Arash Dabirzadeh was born in Esfahan, Iran in 1982. He received his Bachelor of Science degree with honors in Electrical Engineering from Amirkabir University of Technology (Tehran Polytechnic) in 2005 and Master of Science degree in Electrical Engineering from Texas A&M University in 2008. His research/career interests include RF/microwave circuit/coil design for medical imaging.

Mr. Dabirzadeh may be reached at the Department of Electrical and Computer Engineering, 111A Zachry Engineering Building, College Station, TX 77843-3128 or via email at arashdb@gmail.com.